PyroCLAST: a new experimental framework to investigate overspilling of channelized, concentrated pyroclastic currents

V. Gueugneau, S. Charbonnier, Olivier Roche

PyroCLAST: a new experimental framework to investigate overspilling of channelized, concentrated pyroclastic currents

V. Gueugneau[1], S. Charbonnier[1], O. Roche[2]

[1]University of South Florida, School of Geosciences, Tampa, FL, USA
[2]Université Clermont Auvergne, CNRS, IRD, OPGC, Laboratoire Magmas et Volcans, F-63000 Clermont-Ferrand, France

Corresponding author: Valentin Gueugneau (vgueugneau@usf.edu)

Key Points:

- Overspilling of channelized pyroclastic currents is a significant threat for population around volcanoes and remains poorly known
- First experimental device built to investigate the overspilling of pyroclastic currents
- We observe two types of overspills at the passage of a bend in the experimental channel

Abstract

Small-volume concentrated pyroclastic currents (CPCs) are often responsible of unpredicted and deadly overspills from channel confines when they encounter an abrupt change in propagation direction. We present the first results obtained with a new experimental facility, PyroCLAST, built to investigate the mechanisms of such overspills. The apparatus consists of a 5 m long flume with a 45° valley bend at mid-distance from the source, and whose slope angle varies from 3 to 15°. Glass beads of 45-90 µm diameter are initially fluidized in a reservoir and rapidly released into the flume through a vertical sliding gate. Experiments are recorded using video cameras to measure the temporal evolution of both the parent channelized and overbank flow velocity and discharge rate, using Particle Image Velocimetry. Overspills are generated when the flows interact with the bend, at slope angles of 9 to 15°, generating a front splash and an overbank flow. Results demonstrate that the slope angle favors the formation of overspill by increasing the flow discharge rate, causing a local increase of the flow thickness along the bend (i.e. superelevation) that overtops the channel sidewall. Moreover, under constant initial conditions, high channel slope angle and discharge rate favor the development of discrete, internal flow pulses, and a positive correlation is found between the runout of the channelized flows and that of overbank deposits. Data collected in this study will also constitute a reference dataset for future benchmarking of CPC numerical models.

Competing Interests: Authors declare no financial or non-financial interests that are directly or indirectly related to this work.

1 Introduction

1.1. Concentrated pyroclastic currents

Small-volume (usually < 10^7 m^3) pyroclastic currents are complex and dangerous volcanic gravitational flows, composed of a hot mixture of gases and particles and generated from lava dome or small column collapse (Brown and Andrews 2015; Lube et al. 2020). They are capable of flowing over distances typically longer than 3 km and at speeds up to >100 km h^{-1} (Brand et al. 2014; Cole et al. 2015; Pollock et al. 2019). Our study focuses on Concentrated Pyroclastic Currents (CPCs), which are two-layer flows composed of a concentrated basal layer (more than ~40-60 vol.% of particles and an overriding dilute upper layer (less than ~1 vol.% of particles) also called the ash-cloud surge (Dufek et al. 2015; Lube et al. 2020). We do not address dilute pyroclastic currents (DPCs) that only exhibit a dilute layer with a bedload region (Dufek et al. 2015; Valentine, 2020; Brosch and Lube 2020).

The basal part of small-volume CPCs tends to be channelized in deep and narrow valleys of volcanoes. They exhibit remarkably long flow runouts compared to other geophysical granular flows of similar volume (Dade and Huppert 1998; Druitt, 1998; Calder et al. 1999; Iverson and Vallance 2001). Previous studies on CPCs have demonstrated that channelization can enhance flow runout by confining the entire mass into a restricted area, preventing rapid lateral spreading and efficient energy dissipation (Woods et al. 1998; Calder et al. 1999; Andrews and Manga 2012; Jessop et al. 2012; Charbonnier et al. 2013; Ogburn et al. 2014; Aravena and Roche 2022). Furthermore, a high interstitial gas pore pressure and related fluidization in the concentrated basal layer has been proposed as an efficient mechanism to reduce the inter-particle friction and also enhance flow runout (Sparks 1978; Wilson 1980; Druitt et al. 2004; Bareschino et al. 2007; Dufek 2016; Lube et al. 2020), as demonstrated by numerous experimental works (Druitt et al. 2007; Girolami et al., 2015; Roche et al. 2010; Rowley et al. 2014; Smith et al. 2018, 2020) and numerical studies (Gueugneau et al. 2017; Breard et al. 2019, 2022; Lube et al. 2019; Aravena et al. 2021). The rapid decrease of pore pressure at coarse flow margins during emplacement and self-channelization of CPCs can explain deposit structures like lateral static levées and steep front lobes (Wilson and Head 1981; Gueugneau et al. 2017; Smith et al. 2018, 2020; Brand et al. 2017). A better understanding of the effect of channelization and friction reduction in small-volume CPCs is crucial to better estimate their inundation area, and consequently improve the assessment of hazards they pose along valleys of CPC-generating volcanoes.

1.2. The overspill hazard of small-volume CPCs

Even though small-volume CPCs are channelized in valleys of volcanic edifices, most of fatalities are due to the unpredicted overspill of the flows from the channel confines and a rapid inundation of the

interfluves, as the overspills can travel up to a few kilometers from its overflow point (i.e. Volcan de Fuego in 2018; Albino et al. 2020). As detailed in Gueugneau et al. (2021), Kubo Hutchison and Dufek (2021), and Lerner et al. (2021), CPC overspills exhibit various depositional and dynamical characteristics, and here we distinguish two different types:

(i) 'CPC overspill', when the concentrated basal layer of a CPC escapes the valley at a specific location, usually, but not always, accompanied by its upper ash-cloud surge. This overspill continues to flow along valley banks, volcaniclastic terraces and interfluves, and is usually named *overbank flow* to distinguish it from its parent *valley-confined flow*, as at Merapi during the 2006 or 2010 eruptions (Charbonnier and Gertisser 2008; Lube et al. 2011; Gertisser et al. 2012; Charbonnier et al. 2013), at Volcán de Colima (Mexico) in 2015 (Macorps et al. 2018) or at Fuego volcano in 2018 (Albino et al. 2020) (Table 1).

(ii) 'ash-cloud surge detachment' when only the dilute ash-cloud surge decouples from the concentrated basal layer and escapes the confining valley to propagate on its own, as at Montserrat in 1997 (Druitt et al. 2002; Loughlin et al. 2002; Ogburn et al. 2014), Unzen in 1991 (Nakada and Fujii 1993), Merapi in 2010 (Komorowski et al. 2013) or Mount Pelée in 1902 (Gueugneau et al. 2020).

The physics behind CPC overspills remain poorly known despite their danger. Most of our knowledge is based on field studies of CPC deposits (Charbonnier and Gertisser 2008; Lube et al. 2011; Gertisser et al. 2012; Charbonnier et al. 2013; Ogburn et al. 2014; Lerner et al. 2021). These have pointed out that a sudden change in the channel geometry (both from natural causes or the result of human intervention) can potentially reduce the channel capacity, then causing the CPC to overspill. At least four principal topographic features can be distinguished (Table 1):

(a) a sharp valley bend (Ogburn et al. 2014; Macorps et al. 2018),

(b) a break in slope along the valley (Bourdier and Abdurachmann 2001; Charbonnier and Gertisser 2012),

(c) an obstacle obstructing the valley (i.e. sabo dam, lava ridges, or bridges; Charbonnier and Gertisser 2008; Lube et al. 2011).

(d) a sudden reduction of the valley width (i.e. constriction; Charbonnier and Gertisser 2008, 2011; Jenkins et al. 2013)

Recently, Kubo Hutchison and Dufek (2021) and Gueugneau et al. (2021) numerically studied the overspill mechanism. Kubo Hutchison and Dufek (2021) have demonstrated that a sinuous valley can cause an important increase of the local flow thickness along the outside of a bend, called superelevation, leading to the overspilling of the channelized flow. Such sudden superelevation was also inferred from field studies at Merapi in 2006 (Charbonnier and Gertisser 2008; Lube et al. 2011). Gueugneau et al. (2021) highlighted the link between the increase of the local CPC volume flux (calculated along the cross-sectional area of the channel) and the occurrence of an overspill. Unsteady flow conditions and increase in flow velocity, thickness, and volume flux can also promote overspilling (Charbonnier et al. 2013; Kubo Hutchison and Dufek 2021). These studies suggest that the CPCs properties (volume, flow rate) and the geometry of the valley are key parameters controlling overspills. A deeper understanding of the interaction between the valley-confined CPCs and the topography, as well as the evolution of the internal flow conditions during emplacement, is needed to better characterize the mechanisms of CPC overspills and better assess related hazards.

The interaction between channelized flows and topographic obstacles, such as an oblique plane or a vertical wall, has long been studied experimentally for water-particle flows (Armanini and Scotton 1993; Armanini et al 1997, 2010; 2020) or non-fluidized granular flows (Gray et al. 2003; Gray and Cui 2007; Cui et al. 2007; Pudasaini et al. 2007). This issue was discussed for geophysical flows such as snow avalanche, landslides, debris flows or mud flows to properly design protective structures in mountainous areas (Mancarella and Hungr 2009; Ashwood and Hungr 2016; Iverson et al. 2016; Faug 2021). Although being of primary importance in the process of CPC overspill, the interaction between CPCs and topographic obstacles has never been studied experimentally. The laboratory-scale devices of Roche et al. (2010), Rowley et al. (2014), Smith et al. (2018) consist of straight horizontal flumes aimed to investigate the internal and depositional processes of CPCs in a confined configuration. On a larger scale, the 20 m long apparatus PELE (Lube et al. 2015) and the 11 m long apparatus GRANFLOW-SIM (Bartali et al. 2012, Sulpizio et al. 2016) are straight inclined flumes with a constant slope angle, which are terminated by unconfined flat areas. Hence, none of these existing experimental apparatuses admits a non-straight channel morphology with bends or obstacles, neither flat channel banks to receive an overflow. In this context, a new experimental setup with a non-straight channel morphology is necessary to investigate the interaction between a channelized CPC and a valley bend, and to serve as a benchmark for CPC numerical models (Gueugneau et al. 2020).

1.3. Aims of the study

Here we present the first results of laboratory experiments carried out with a new facility called PyroCLAST (Pyroclastic Current Large-scale Apparatus using Synthetic Topographies) and built to investigate CPC overspills. This study focuses on the relation between the dynamics of channelized parent flows, the occurrence of an overspill, and the dynamics of the overbank flow. In this study, we consider a sharp valley bend (i.e., the most common topographic feature, see Table 1), simplified here by a double 45° bend in opposite directions (see Fig. 1a) and positioned half-way along a 5 m long flume. To explore a broad range of flow conditions at the overspill site, the slope angle is modified from 3 to 15°, while keeping the same initial mass of granular material. We consider initially fluidized granular flows (i.e., with interstitial pore fluid pressure), which are obtained by injecting a vertical air flow at the base of a granular bed in a semi-closed reservoir prior to release into the channel. The properties of the channelized and overbank flows (i.e., front and internal velocity, flow thickness and discharge rate), as well as the final deposit morphology (i.e., deposit length and thickness), are measured during and after each experimental run, respectively. We first describe the design and conception of the apparatus, and the experimental procedure for each experiment, before presenting the results of the first set of experiments. Results are discussed and put into perspective with previous experimental results of channelized granular flows, but also with natural CPCs.

A complementary goal of this project is to build a new experimental database for the benchmarking of numerical models for pyroclastic currents, recently initiated by an international community effort presented in Esposti Ongaro et al. (2020). The first synthetic benchmarks for CPC models conducted by Gueugneau et al. (2021) showed that using a robust reference database to compare models is required to estimate their robustness in simulating channelized CPC processes.

2 Materials and methods

2.1. Preliminary analysis

We first present a simple energy balance for an inviscid fluidized granular flow (i.e., with negligible dissipative stresses) in a channel with an obstacle of height Δz by considering the conversion of the flow kinetic energy to the potential energy (Fig. 2a). We considered this analysis to design PyroCLAST. For a finite flow mass m, the kinetic energy needed by the flow of velocity v_p perpendicular to the obstacle to raise the height Δz satisfies

$$\frac{1}{2} m {v_p}^2 = mg\Delta z, \quad (1)$$

where g is the gravitational acceleration, so that

$$v_p = \sqrt{2g\Delta z}\,. \quad (2)$$

This only applies if Δz is significantly larger than the flow thickness. We consider now a bend in a channel with an angle A (Fig. 2b). In this configuration, the velocity component v_p perpendicular to the bend sidewall (green arrow, Fig. 2b) as a function of the flow velocity v and the bend angle is

$$v_p = v\sin(A)\,. \quad (3)$$

Therefore, combining equations (2) and (3), the minimum velocity needed for an inviscid and incompressible thin flow to overtop the channel bend is:

$$v = \frac{\sqrt{2g\Delta z}}{\sin(A)}\,. \quad (4)$$

If we further consider the slope angle α of the channel as shown in Fig. 2c, projected vertical sidewall height is

$$h = \Delta z\cos\alpha\,, \quad (5)$$

and the minimum flow velocity to climb this height is

$$v_\alpha = \frac{\sqrt{2g\Delta z\cos\alpha}}{\sin(A)}. \quad (6)$$

This theoretical flow velocity is an approximation of the minimum velocity needed to raise the thin flow and potentially generate an overspill since it does not take into account the energy lost by interparticle and particle-wall collisions or friction at impact. The minimum velocity v_α decreases slightly from 2.42 to 2.38 m s^{-1} as the slope angle increases from 0 to 15°, while it decreases significantly when the angle of the bend increases (Fig. 2d-e). As a comparison, the maximum velocity of an inviscid gravitational thin flow on a straight slope varying from 0 to 15°, calculated using equation (2) and (5) with Δz the height difference between the starting point and the lowest point of the flow (front), is between 2.2 to 5 m s^{-1}. Because this maximum flow velocity is nearly equivalent or superior to v_α in a channel with 15 cm high walls and a 45° bend for the same slopes, this configuration should allow gravitational thin flows to overtop sidewalls at the bend, and therefore was chosen for our PyroCLAST apparatus.

2.2. Design of the apparatus

PyroCLAST is designed in a dam-break configuration, for which a granular bed confined in a reservoir is suddenly released in a flume at various inclinations. Many experimental studies in volcanology have considered this configuration (e.g., Roche et al 2010; Sulpizio et al. 2016; Smith et al. 2018), because it allows the generation of rapid dense granular flows, in particular with high Froude numbers and other dimensionless parameters, required to simulate natural CPCs (see Table 2).

To investigate the overspilling of CPCs with our apparatus, the channel morphology was chosen to mimic a valley bend typical of a volcanic edifice (see Table 1). Hence, we designed PyroCLAST with three main elements (Fig. 3): a reservoir that contains the granular material before an experiment, a 1.8 m long channel with transparent Plexiglas walls that confines the flow after releasing the granular material, and a 3 m long low profile channel that comprises the topographic feature. This distal channel section is the key element in the apparatus. To allow flow overspills, and following our preliminary analysis, the second channel has 15 cm high sidewalls and a 45° bend at a distance of 3 m from the reservoir, followed by another similar bend in the opposite direction 0.55 m downstream. Overspills generated at the first bend spread on a large inclined plane. The inclined plane, made of wood, allows a rapid and easy modification of the channel morphology for future studies.

The channel slope angle can be varied from 3 to 21° by vertically lifting the reservoir within a metal frame, changing the inclination of the two channel sections (Fig. 3). An experiment is triggered by the rapid lifting of a sliding gate that separates the reservoir from the first channel, activated by the vertical fall of a 30 kg sandbag at the rear of the apparatus. To allow the granular material to be initially fluidized, the base of the reservoir consists of a porous plate (2 cm thick, mean diameter of the pores of 20 µm) through which an air flow is injected and maintained throughout the experiment. This permits us to generate pore fluid pressure, which in nature can result from various mechanisms involving particles and gas moving downward and inward respectively. The total thickness of the reservoir base, called the windbox, is 7.6 cm (porous plate included).

2.3. Experimental procedure

We chose to focus our experiments on the influence of the initial pore pressure and the slope angle on the dynamics of the channelized flow and overspill generation. We selected five slope angles, 3, 6, 9, 12 and 15°, at which three to five experiments with initially fluidized granular material were run. In addition, three non-fluidized experiments at 9 and 12° were performed for comparison with those involving initial pore pressure. Experiments were recorded using four GoPro cameras and one high-speed camera to investigate the flow front position and velocity of both the parent channelized and overbank flows. The

flow front position was measured by correlating each GoPro video frame at different locations across the channel length. Images recorded with the high-speed camera at 1000 frame/s (dashed red square in Fig. 4a-c) were analyzed by Particle Image Velocimetry (PIV) using PIVlab on Matlab (Thielicke et al. 2021). The flow thickness (Fig. 4b-d) and flow velocity profiles at the sidewall (Fig. 4d) were measured for each frame at 1.5 m from the reservoir (vertical black line, Fig. 4a-b). By integrating the velocity profile over the flow thickness for each frame (Fig 4c-d), we deduced the temporal evolution of the volume flux at that particular location. Note that this discharge rate is an approximation as the flow velocity varies across the channel due to wall friction (Fig. 4c).

We used synthetic, subspherical borosilicate glass beads of 45-90 μm diameter (Table 1 in Supplementary Material). We chose this material because it has several advantages compared to natural PCs particles: (i) it is well sorted and contains negligible amount of very fine (<20 μm) particles and is therefore simple to fluidize at laboratory scale (i.e. negligible cohesion effect), easy to use and recycle, and does not pose a health hazard, and (ii) their internal properties are well-known (i.e., density, shape and grain size distribution), which help characterizing physical processes involved during flow emplacement. The glass beads have a density of ~2500 kg m^{-3}, while granular beds have a bulk density of ~1500 kg m^{-3} with solid volume fraction of ~0.6. We chose a constant bulk volume of particles of 0.09 m^3, corresponding to a mass of ~135 kg of beads with a bed height of 40 cm in the reservoir. The beads belong to the group A of Geldart's classification (Geldart 1973), meaning that the granular bed is fully fluidized (i.e. pore fluid pressure equal to the lithostatic pressure) at the minimum air fluidization velocity U_{mf} with negligible expansion. In our experiments U_{mf} is 0.01 m s^{-1}, corresponding to an air flow rate of about 0.5 m^3 s^{-1} (measured at onset of bed expansion) supplied by a compressor equipped with a dryer unit. To avoid particle cohesion effects caused by the ambient air humidity, particles were dried in an oven at 80°C during 40 to 90 hours prior to each experiment, depending on the degree of humidity of the room, before being immediately loaded into the reservoir a few minutes before the experiment. For all experiments of this study, the initial temperature of the granular medium was 50-60°C, while the ambient temperature and the relative humidity were 19-21°C and 55-60 %, respectively.

3. Results

3.1. Dynamics of channelized flows

We first analyze the channelized flow kinematics at varying channel slope angles and with or without initial pore pressure. The position of the front of the initially fluidized flows (measured along the channel central axis) and the corresponding flow front velocities are shown in Fig. 5a-b. For comparison, the front positions and velocities of non-fluidized flows with 9 and 12° channel slope angles are also presented. To

allow the comparison with future experiments and numerical model benchmarking, the front position is normalized by the initial height of the granular bed in the reservoir h_0 = 0.4 m. Results show that at channel slope angles of 9-12° (i.e., only comparable angles between the two types of flows), the normalized flow runout increases from x/h_0 = 2.5-3 for non-fluidized flows to x/h_0 = 4-5 for initially fluidized flows.

The front velocity v_f of initially fluidized flows reveals distinct phases (Fig. 5b): (i) a first phase of acceleration during ~0.15 s after release, then a short period of nearly constant velocity during ~0.1s, and a second stage of acceleration until ~0.5 s on average (notice that all experimental flows show about the same temporal evolution); (ii) a transitional phase during which the flows have different kinematics depending on the channel slope angle: another stage of acceleration at 12 and 15°, a constant velocity at 9° and 6°, or a deceleration at 3°; (iii) an impact phase during which the flows interact with the oblique side of the channel bend, causing a short but rapid drop in the flow velocity; (iv) a constant deceleration phase until the flows stop, except for experiments at 12 and 15° channel slope angles for which another acceleration of the flow front is observed after the bend at 1.5-2 s, followed by a final constant deceleration. Note that the second stage of acceleration during phase (i) for all experiments, and the terminal velocity peak observed after 2.5 s for experiments at 15° slope, are caused by surface waves, which are clearly visible on videos, travelling faster and eventually overtaking the flow front, as observed in debris flow experiments (Zanuttigh and Lamberti 2007). Surface waves push the flow front further donwstream, increasing the maximum flow runout that draws a linear relationship with the channel slope angle (Fig. 5d).

To better characterize the regime of our experimental flows, we calculated the Froude number of the flow front $Fr_{front} = \frac{v_f}{\sqrt{H\ g\ cos\alpha}}$, with α the slope angle, g the gravity, v_f the flow front velocity, and H the vertical flow thickness (Fig. 5c). A mean flow thickness of 0.05 m is set as the characteristic thickness H, obtained by averaging the thicknesses at the flow heads in Fig. 5e, as described hereafter. The flow front velocity and the front Froude number show similar temporal evolutions, in particular with Fr >> 1 during most of the flow emplacement. These values of Froude number indicate that the flows are supercritical and mostly driven by their inertia, except at very late depositional stages, and therefore prone to surface wave formation as confirmed by our observations.

To further characterize the flow dynamics, we present in Fig. 5e-h PIV measurements, at 1.5 m from the reservoir, of the temporal flow thickness, the mean velocity at sidewall v_s, and the flow discharge rate. In addition, the internal Froude number $Fr_{flow} = \frac{v_s}{\sqrt{H\ g\ cos\alpha}}$ calculated from v_s the mean velocity at sidewall (Fig. 5f), is also presented. Overall, the higher the channel slope angle, the higher the flow velocity and flow discharge rate. The flows exhibit important variations in their thickness and velocity, enabling us to differentiate a head, a body and a tail. For each channel slope angle, these flow properties show similar patterns as shown in Fig. 5e-f: (i) when the flow front reaches the probing area, the thickness rapidly

increases and reaches a first plateau (increasing with the slope angle), while the mean velocity v_s also increases rapidly and reaches a maximum value that increases as the channel slope angle increases (up to 1.2 m s^{-1} on average at 15°); (ii) following this plateau, the thickness increases again, which marks the transition to the flow body with maximum flow thicknesses; (iii) after the passage of the body, the flow thickness remains constant for the low to medium slope angles (<9°), but shows a decrease of up to 30% for the steepest slopes (12 and 15°), while the flow velocity decreases in each case. We identify this last phase as the passage of the tail of the flow. By integrating the flow velocity along the flow height with the channel width, the evolution of the flow discharge rate (DR) is obtained (Fig. 5h). Two well developed peaks in discharge rate reflect the passage of the flow head and the flow body. The higher the channel slope angle, the higher the DR, causing stronger second peaks of discharge rates at high slope angles. We will discuss below the correlation between this second peak in the DR and the generation of overbank flows.

3.2. Generation of flow overspill

We have observed flow overspills at the passage of the channel bend only for initially fluidized flows and at varying slope angles from 9 to 15°. Two different types of flow overspill can be distinguished: (i) a front splash after the passage of the flow front, forming a thin immobile deposit < 3 mm; (ii) a second overspill, which we call overbank flow, occurring after the front splash in experiments with 12 and 15° channel slope angles.

The front splash is caused by the complex behavior of the flow front interacting with the bend section: it runs up vertically along the bend sidewall, in a jet-like behavior as previously described for wet granular flows impacting a vertical wall (Armanini and Scotton 1993; Armanani et al. 2010) and is simultaneously deflected laterally. Once the jet reaches its maximum height, its falls back on the channel bank and transitions into a reflected wave inside the channel, also observed in wet granular flows experiments (Armanini and Scotton 1993; Armanani et al. 2010; Iverson et al. 2016). The wave rolls laterally and falls on the flow's free surface, parallel to the bend side wall (Fig 6a). When the front has passed the obstacle at slope angles 12-15°, the overbank flow starts forming at the first bend and propagates on the bank in the same direction as the main channel axis (see arrows in Fig 6b-d.). It reaches its maximum runout approximately at the middle of the bend, and its outer limit is subparallel to the bend sidewall. The thickness of the overbank flow deposit varies from ~0.2 cm at the front to ~3 cm along the edge of the channel at 15°.

The formation of these flow overspills is related to varying channelized flow conditions and occurs at very specific periods during the emplacement of the parent flows. By carefully observing the videos of each experiment, we can define a flow overspill sequence (Fig. 7):

A) The very thin and fast flow head reaches the bend.

B) The flow front impacts the oblique channel wall and propagates both vertically and laterally, causing the formation of a roll back wave. This also causes an important variation of the flow

thickness across the channel, with a flow height along the impacted side higher than along the opposite side of the bend. In the following, we name this local and rapid thickness increase a *superelevation*.

C) For experiments at 3 and 6° slope, the jet height is lower than the channel bank height and no overspill occurs. However, at 9° or higher, the jet height exceeds the channel wall height and the granular material overflows on the channel banks, towards the distal bend section (see Fig. 6), to create a front splash that immediately freezes.

D) For experiments at 12° slope and higher, the front roll back wave inside the channel slowly transitions to a granular jump (Gray et al. 2003; Gray and Cui 2007) at the beginning of the bend. Simultaneously, the flow thickness along the impacted side of the bend rapidly increases and finally exceeds the channel height. This causes the channelized flow to overspill on the channel bank to form a secondary flow. The later initiates first at the proximal point of the bend, and propagates downstream over the channel bank as an overbank flow, while its flow direction is that of the straight channel axis (see also Fig 6.). Note that the granular material does not reach the opposite side of the bend from the onset of the overbank flow until almost the end of the flow propagation.

3.3. Overbank flow dynamics

Overbank (OB) flows occurred at 12 and 15° channel slope angles (Fig. 8a-b). As for their parent channelized flows, OB flow runout distance increased significantly when the slope increased, from x/h_0 = 0.5 – 1 at 12° to x/h_0 = 1.8 – 2.1 at 15° (Fig. 6a). However, the temporal evolution of the velocity of OB flows differs significantly from that of the parent channelized flows since OBs do not interact with any obstacle but spread on an unconfined inclined surface. In fact, these OB flows share some similarities with the non-fluidized channelized flows (Fig. 5a-b): an initial acceleration phase followed by a short constant velocity phase and then a constant deceleration. However, the Froude number at the front $Fr_{f\_OB} = \frac{v_{fOB}}{\sqrt{H\ g\ cos\alpha}}$ = ~2-5, with a typical thickness H=0.01 m (approximately the average thickness of OB flows), is closer to that of the parent channelized flows (Fig. 8c). This shows that OB flows are also supercritical and therefore prone to surface wave instabilities (Fig. 6c-d).

There appears to be a correlation between the slope angle and the runout of the OB flows (Fig. 8d). In contrast, the maximum extent of front splashes shows significant variability with the slope angle. OB flows properties are dependent on those of their parent channelized flows. There is a good correlation (R^2 = 0.89) between the channelized flow runout R_{cf} and the OB flow runout R_{ob} (Fig 8e):

$$R_{ob} = 1.5\ R_{cf} - 7.4 \quad (7)$$

This shows that for $R_{ob} = 0$, the minimum channelized flow runout required to generate an overspill is $R_{cf} = C/1.5 = 4.9\ m$. Equation (7) shows that the occurrence and runout of an OB flow can be expected from the parent channelized flow properties.

4. Discussion

4.1. Influence of the slope angle on channelized flow dynamics

We discuss the dynamics of our experimental flows in light of earlier studies on confined granular flows of spherical particles and with smooth boundaries. Theoretical (Brodu et al. 2015; Zhu et al. 2020) and experimental (Louge and Keast 2001; Holyake and McElwaine 2012; Heyman at al. 2017; Roche et al. 2021) works have revealed a richness of flow dynamics, which depends essentially on the channel slope angle and the balance between driving gravitational forces and resisting forces at the smooth rigid boundaries (i.e., the channel base and lateral walls). After release, the granular material accelerates, decelerates and stops if the slope angle is less than ~15°. At steeper slope angles, the flow accelerates and propagates in a so-called immature regime until it acquires a steady fully-developed (SFD) regime once resisting forces balance driving forces. The transition from the immature to the SFD flow regime occurs at longer distance as the slope angle increases. SFD flows have a dense core caused by inelastic collapse of the expanded granular material, but lower particle concentrations at their boundaries, which is a signature of a supported flow regime, and they often exhibit longitudinal rolls (Brodu et al 2015). As shown by both theoretical (Zhu et al. 2020) and experimental (Roche et al. 2021) investigations, the effective friction coefficient (μ) of these flows with smooth boundaries increases with the slope angle and it depends essentially on a dimensionless number analogous to a Froude number (Fr). Interestingly, the μ(Fr) curve for these plug-like flows with high shear velocities along the smooth boundaries shares strong resemblance with the μ(I) rheological curve for granular flows over rough substrates and with negligible slip velocities (cf. Breard et al. 2022). We rely on these findings to discuss our experimental results. We acknowledge, however, that care must be taken regarding the interpretation of the dynamics of confined, initially fluidized flows with smooth boundaries whose physics have not yet been investigated in detail, in contrast to non-fluidized flows. Our experiments were carried out at gentle slope angles ≤15°. Therefore, the non-fluidized flows remained in the immature regime and stopped in the straight upper channel upstream the bend. In contrast, initially fluidized flows, with their reduced internal stresses (cf. Breard et al. 2022), could reach the bend, either in the immature (12 and 15°) or the SFD (3, 6 and 9°) regimes. Then, their dynamics changed drastically through interaction with the bend and they eventually stopped downstream. In a straight channel, these flows might have reached the SFD regime (12 and 15°) or remained steady (3, 6 and 9°) for a while before they would have behaved as non-fluidized flows once defluidized.

Results obtained with initially fluidized flows show a proportional relationship between channel slope angle and flow runout (Fig. 5d). This proportionality has already been demonstrated in previous studies for confined non-fluidized (e.g. Pouliquen 1999; Gray et al. 2003; Pudasaini et al. 2007) or fluidized flows with similar channel slope angles (< 20°; e.g. Chédeville and Roche 2015; Aravena et al. 2021). The runout of initially fluidized flows increases by a factor of ~2 from 3° to 15° slope angles, in agreement with the simulations of Aravena et al. (2021) and with the experiments of Chédeville and Roche (2015). In the latter publication, the authors show that the runout increases exponentially beyond channel slope angles of 15-20°, which have not been explored in our study. However, simulations of Aravena et al. (2021) show that the increase in runout distance may be self-limited at increasing channel slope angle because the high flow velocity due to fluidization causes lateral spreading of the flow and rapidly reduces its thickness, which induces faster pore pressure diffusion and transition to the non-fluidized flow regime.

4.2. Flow interaction with the channel bend

The front splash overspill occurs at slope angles ≥ 9° when the flow front impacts the bend and rises vertically before falling back both on top of the channelized flow and on the channel bank. The presence of a reflected wave is in agreement with the experiments of Armanini and Scotton (1993) and Armanini et al. (2010) who have demonstrated that flows with Fr >1 tends to form thin and fast fronts that run up the obstacle in a jet like behavior, which transition to a reflected wave eventually. These results suggest that our initially fluidized flows had a fluid-like behavior at least until the impact with the channel bend.

As shown by our simple analysis with the thin flow theory in section 2.2., the minimum front velocity of an inviscid flow needed to generate a vertical rise of 15 cm along an oblique 45° channel bend decreases from 2.42 m s^{-1} at 3° slope angle to 2.39 m s^{-1} at 15°. Since fluidization drastically reduces effective friction, and that the experimental flow front thickness (~ 1 cm) is much smaller than the channel depth, we can postulate that our initially fluidized experimental flows behave as inviscid thin flows, and that pore pressure has not decreased significantly at the time of impact with the bend. Measured flow front velocities (Fig. 9a) are ~0.5-1 m s^{-1} higher than the theoretical minimum velocity v_p obtained from equation 6 (blue dashed line, Fig 9a), suggesting that experimental flows have enough energy before the impact to overtop the channel wall, even at 3° slope angle. The theoretical height *H* the experimental flows could reach calculated from equation 6, with a channel angle ϑ,

$$H = \frac{(\sin(\vartheta)v)^2}{2g\cos\alpha} \quad (8)$$

is ~10-16 cm higher than the 15 cm height of the channel sidewall (black dashed line, Fig. 9b). However, as seen in section 3, flow overspills are only observed at channel slope angles ≥9°. Therefore, our data suggest that at impact with the oblique channel wall at the lowest slopes angles of 3 and 6°, (i) pore fluid pressure has decreased significantly (because of smaller flow velocities and thicknesses compared to higher slope angles) and/or (ii) energy dissipation through collisions between the particles and with the sidewall was non-negligible. In fact, the flow energy was high enough to cause overspill only in experiments at slope angles ≥9°, and we can define the minimum velocity to generate an overspill with our configuration between 2.9 and 3.1 m s^{-1} (Fig. 9a).

An overbank flow follows the front splash in experiments with 12° and 15° channel slopes, because the thickness of the flow body increases to the point that the flow overspills on the channel bank. This sudden thickness increase is due to several factors. The thickness variation of a granular flow impacting an obstacle has been studied in earlier experimental works. A granular jump was observed for granular flows at Fr>1 impacting an obstacle perpendicular (Gray et al. 2003; Pudasaini et al. 2007) or oblique (Cui et al. 2007; Gray and Cui 2007) to the direction of flow propagation. Gray et al. (2003) and Pudasaini et al. (2007) showed that the granular jump increases rapidly in thickness after impact and propagates upslope, similarly to pure fluid flows (Savage and Hutter 1989). Gray et al. (2003), and later Tiberghien et al. (2007), Faug et al. (2012) and Caccamo et al. (2011, 2012), showed that a granular jump can evolve into a basal stagnation zone (i.e., where the granular material is static) overlain by the flowing material, which overtops the obstacle. Our experimental flows with Froude numbers of 3-5 were prone to granular jump. However, we could not investigate this phenomenon because the channel side walls at the bend were not transparent. Furthermore, the frontal roll back wave fell back onto the flow (see Fig. 7) and the flow discharge rate was not constant. These two processes did not permit us to investigate in detail the variation of flow thicknesses at the impact with the bend and, therefore, prevented us from documenting the dynamics of the granular jumps.

4.3. Implications for natural PCs and perspectives

Our experiments involving a simple configuration suggest that a channel bend can be very efficient to cause overspill of CPCs. We have demonstrated that an initially fluidized granular flow impacting an oblique channel wall can generate an overspill, even when propagating on gentle slopes ≤15°. Overspill can occur even if the channelized flow does not fill the entire channel width (Gueugneau et al. 2021; Kubo Hutchison and Dufek 2021). Future studies on CPCs overspill and evaluation of channel capacity should focus on determining the conditions that promote the formation of a superelevation wedge in the vicinity of a sudden topographic change. Using up-to-date, high-resolution DEMs, an automatic recognition of

hazardous overspill zones along valleys of PC-generating volcanoes from numerical simulations could lead to a new generation of enhanced and dynamic hazard and risk maps. The fact that a granular jump is one of the factors contributing to the formation of overbank flows confirms the ability of shallow-water numerical models to simulate CPC features, since such models are able to reproduce hydraulic jumps (as seen for example in Gueugneau et al. 2021). The possible presence of a basal stagnation zone, however, would require the use of other modeling approaches, such as two-phase continuum (Aravena et al. 2021), multiphase discrete element (Lube et al., 2019; Breard et al., 2022) or smooth-particle hydrodynamics (Zhu et al., 2021) simulations.

Further experimental studies should address some key parameters in more detail. First, the channel geometry: as shown by earlier studies, the angle and the sinuosity of the bend (Peruzzetto et al. 2021; Kubo Hutchinson and Dufek 2021) as well as the shape of the topographic feature (obstacle, break in slope, constriction; Gueugneau et al. 2021) control the generation and type of overspills. Comparison with the results of other existing experimental facilities such as that of Sulpizio et al. (2016), for which flows are only confined along half of their path, could better constrain the effect of flow confinement on the flow runout. It would be also important to run experiments with polydisperse granular materials, in order to investigate the dynamics of two-layer flows, and in particular the detachment of the upper dilute part at impact with the different topographic features (Fig. 1).

Finally, our study provides an experimental dataset for current and future benchmarking initiatives of mass flow models. The PyroCLAST apparatus can be used in future studies to (i) improve our capability of assessing PC inundation zones over complex topography by investigating the interplay between the PC dynamics and their responses to topographic changes, and (ii) quantify how changes in topography can modify the local flow rheology. A cross comparison with other large-scale facilities specifically designed to study the effect of channelized flows at break-in-slope (Sulpizio et al. 2016) is also another potential application with PyroCLAST.

5 Conclusions

We observed two types of flow overspills from experimental, initially fluidized channelized granular flows over low to medium channel slope angles (9° to 15°) and interacting a 45° oblique bend: i) a front splash at the impact of the flow front with the bend, and ii) an overbank flow at the passage of the flow body, provided the slope angle was high enough (12 and 15°). Results of our experiments have demonstrated that the slope angle enhances the channelized flow runout and favors the formation of overspills at the bend, due to faster flow propagation and related mass flow rate. The flow velocity is the

key parameter, and in the configuration chosen, a minimum flow front speed of ~2.9 - 3.1 ms^{-1} is required to generate overspills, which corresponds to a minimum flow runout of ~4.9 m in the channel. The formation and dynamics of overbank flows are linked to the dynamics of their parent confined flows, and a correlation exists between their respective flow runouts. Overbank flow is caused by both the formation of a granular jump and a peak in discharge rate due to flow unsteadiness, which contribute to an increase of the granular material thickness along the impacted side of the bend and cause an overspill. The formation of a superelevation wedge should be carefully studied in natural valleys to help define zones of potential hazardous CPC overspills. Finally, the results of this study constitute a dataset for current and future benchmarking of numerical models of CPCs.

Acknowledgments

Financial support was provided by Sylvain Charbonnier's NSF CAREER grant #17511905, including the experimental development at USF's experimental facility. We also thank Greg Valentine for his editorial work, as well as the two anonymous reviewers for their thorough review of our manuscript. This is Labex ClerVolc contribution n° XXX.

Data Availability Statement

Data collected and analyzed in this study are available on the Ghub platform at: XX.

Table 1: Summary of notable CPCs and morphometry of the corresponding channels they flowed into. For each case, the topographic feature identified as responsible for an overspill is described. The morphometry of PyroCLAST is presented in the last row. H/L refers to the ratio between the initial height (H) of the material over the flow runout length (L).

Table 2: Principal dimensionless numbers and parameters for CPCs and PyroCLAST.

Fig. 1 : Illustration of the four main topographic features mentioned to cause a CPC to overspill along volcanic valleys.

Fig. 2 : Analysis of the minimum flow velocity required to climb an obstacle in a channel bend. (a) Horizontal channel with obstacle of height Δz and perpendicular velocity v_p. (b) Horizontal channel with a bend at angle A. (c) Channel inclined at angle alpha. (d-e) Minimum flow velocity v_α required to climb the obstacle, from equation (6), as function of the channel slope angle and the angle of the bend.

Figure 3 : 3D sketches and photographs of the apparatus PyroCLAST: (a) lateral view of the apparatus, (b) view from the end of the channel, (c) 3D sketch in top view of the apparatus showing

the three distinct parts (reservoir, transparent channel, wood channel), (d) 3D sketch showing the three parts in sideview and the reservoir opening system in the back (sand bag).

Figure 4 : Configuration for data acquisition during the experiments. (a) Schematic cross section showing where the PIV measurements are performed (dashed red rectangle). (b) Example of an image processed by PIV to extract the horizontal displacements (green arrows). (c) 3D diagram of the flow configuration in the channel, showing the 3D flow velocity field and the section recorded for PIV. (d) Horizontal flow velocity measured at the channel wall as a function of position from the base, calculated from the PIV frame presented in (b).

Figure 5. Kinematic data of non-fluidized and initially fluidized flows. Temporal evolution of (a) the flow front position x normalized by the initial bed height h0, (b) the front velocity vf, and (c) the front Froude number Frflow. (d) Maximum flow runout as function of the slope angle. Temporal evolution at 1.5 m from the reservoir (calculated using PIV) of (e) the normalized flow thickness, (f) the mean velocity at sidewall v_s, (g) the internal Froude number Frint, and (h) the flow discharge rate.

Figure 6. Sequence of images from the top of the bend section of the apparatus for an experiment with a 12° slope angle, showing two types of overspills: (a) the front splash, and (b-e) the overbank flow that partially covers the front splash. Time t=0 s is defined when the overbank flow starts to spill over in (a).

Figure 7. Diagrams and photographs of an experiment at 12° slope angle illustrating the morphological evolution of the flow front impacting the bend. (a) Fast and thin flow head approaching the bend, (b) flow front impacting the bend and ramping up the channel margin vertically, (c) the front rolls back partially towards the flow inside the channel, while another part overspills on the channel bank, (d) the flow body reaches the bend and causes the flow to overspill and generate an overbank flow.

Figure 8. Kinematic data of the front of the overbank flows. (a-c) Temporal evolution of the normalized flow front position, the front velocity, and the front Froude number. (d) Maximum runout of front splashes and overbank flows as function of the slope angle. (e) Runout of the overbank flows as function of runout of their parent channelized flows.

Figure 9.(a) Theoretical minimum flow front velocity needed to overtop the sidewall (dashed blue line) and measured velocities in experiments (square = measured, red asterisk = average value at given slope angle) as a function of the slope angle. (b) Theoretical height that a flow can reach according to the measured front velocity (squares = calculated value, red asterisk = average value at given slope angle)

References

Albino F, Biggs J, Escobar-Wolf R, et al (2020) Using TanDEM-X to measure pyroclastic flow source location, thickness and volume: Application to the 3rd June 2018 eruption of Fuego volcano, Guatemala. J Volcanol Geotherm Res 406:107063. https://doi.org/10.1016/j.jvolgeores.2020.107063

559 Andrews BJ (2014) Dispersal and air entrainment in unconfined dilute pyroclastic density
560 currents. Bull Volcanol 76:852. https://doi.org/10.1007/s00445-014-0852-4

561 Andrews BJ, Manga M (2011) Effects of topography on pyroclastic density current runout and
562 formation of coignimbrites. Geology 39:1099–1102. https://doi.org/10.1130/g32226.1

563 Andrews BJ, Manga M (2012) Experimental study of turbulence, sedimentation, and
564 coignimbrite mass partitioning in dilute pyroclastic density currents. J Volcanol Geotherm
565 Res 225–226:30–44. https://doi.org/10.1016/j.jvolgeores.2012.02.011

566 Aravena A, Roche O (2022) Influence of the topography of stratovolcanoes on the propagation
567 and channelization of dense pyroclastic density currents analyzed through numerical
568 simulations. Bull Volcanol 84 :7-67. https://doi.org/10.1007/s00445-022-01576-2

569 Aravena A, Chupin L, Dubois T, Roche O (2021) The influence of gas pore pressure in dense
570 granular flows: numerical simulations versus experiments and implications for pyroclastic
571 density currents. Bull Volcanol 83:77. https://doi.org/10.1007/s00445-021-01507-7

572 Armanini A., Scotton P. (1993) On the Dynamic Impact of a Debris Flow on structures.
573 Proceedings of XXV IAHR congress, Tokyo (Tech.Sess.B,III): 203–210.

574 Armanini A, Larcher M, Odorizzi M (2011) Dynamic impact of a debris flow front against
575 avertical wall. Int Conf Debris-Flow Hazards Mitig Mech Predict Assessment, Proc 1041–
576 1049. https://doi.org/10.4408/IJEGE.2011-03.B-113

577 Armanini A, Rossi G, Larcher M (2020) Dynamic impact of a water and sediments surge against
578 a rigid wall. J Hydraul Res 58:314–325. https://doi.org/10.1080/00221686.2019.1579113

579 Ashwood W, Hungr O (2016) Estimating total resisting force in flexible barrier impacted by a
580 granular avalanche using physical and numerical modeling. Can Geotech J 53:1700–1717.
581 https://doi.org/10.1139/cgj-2015-0481

582 Bareschino P, Gravina T, Lirer L, et al (2007) Fluidization and de-aeration of pyroclastic
583 mixtures: The influence of fines content, polydispersity and shear flow. J Volcanol
584 Geotherm Res 164:284–292. https://doi.org/10.1016/j.jvolgeores.2007.05.013

585 Bartali R, Sarocchi D, Nahmad-Molinari Y, Rodríguez-Sedano LA (2012) Estudio de flujos
586 granulares de tipo geológico por medio del simulador multisensor GRANFLOW-SIM. Bol
587 Soc Geol Mex 64:281–291.

588 Bourdier J-L, Abdurachman E (2001) Decoupling of small-volume pyroclastic flows and related
589 hazards at Merapi volcano, Indonesia. Bull Volcanol 63:309–325.
590 https://doi.org/10.1007/s004450100133

591 Brand BD, Mackaman-lo C, Pollock NM, Bendaña S, Dawson B, Wichgers P (2014) Dynamics
592 of pyroclastic density currents : Conditions that promote substrate erosion and self-

channelization — Mount St Helens, Washington (USA). J Volcanol Geotherm Res 276:189–214. https://doi.org/10.1016/j.jvolgeores.2014.01.007

Brand BD, Pollock NM, Sarocchi D, et al (2017) Field-trip guide for exploring pyroclastic density current deposits from the May 18, 1980, eruption of Mount St. Helens, Washington. USGS Sci Investig Rep 2017-5022-C

Breard ECP, Dufek J, Roche O (2019) Continuum Modeling of Pressure-Balanced and Fluidized Granular Flows in 2-D: Comparison With Glass Bead Experiments and Implications for Concentrated Pyroclastic Density Currents. J Geophys Res Solid Earth 124:5557–5583. https://doi.org/10.1029/2018jb016874

Breard ECP, Dufek J, Lube G (2018) Enhanced Mobility in Concentrated Pyroclastic Density Currents: An Examination of a Self-Fluidization Mechanism. Geophys Res Lett 45:654–664. https://doi.org/10.1002/2017gl075759

Breard ECP, Dufek J, Fullard L, Carrara A (2020) The Basal Friction Coefficient of Granular Flows With and Without Excess Pore Pressure: Implications for Pyroclastic Density Currents, Water-Rich Debris Flows, and Rock and Submarine Avalanches. J Geophys Res Solid Earth 125:e2020JB020203. https://doi.org/10.1029/2020JB020203

Breard ECP, Fullard L, Dufek J, Tennenbaum M, Fernandez Nieves A, Dietiker JF (2022) Investigating the rheology of fluidized and non-fluidized gas-particle beds: implications for the dynamics of geophysical flows and substrate entrainment. Granul 24:34.

Brian Dade W, Huppert HE (1998) Long-runout rockfalls. Geology 26:803–806. https://doi.org/10.1130/0091-7613(1998)026<0803:lrr>2.3.co;2

Brodu N, Delannay R, Valance A, Richard P (2015) New patterns in high-speed granular flows. J Fluid Mech 769:218–228. https://doi.org/10.1017/jfm.2015.109

Brosch E, Lube G (2020) Spatiotemporal sediment transport and deposition processes in experimental dilute pyroclastic density currents. J Volcanol Geotherm Res 401:106946. https://doi.org/10.1016/j.jvolgeores.2020.106946

Brown RJ, Andrews GDM (2015) Deposits of Pyroclastic Density Currents. Encycl. Volcanoes 631–648. Elsevier. https://doi.org/10.1016/b978-0-12-385938-9.00036-5

Bursik MI, Woods AW (1996) The dynamics and thermodynamics of large ash flows. Bull Volcanol 58:175–193. https://doi.org/10.1007/s004450050134

Caccamo P, Chanut B, Faug T, et al (2012) Small-scale tests to investigate the dynamics of finite-sized dry granular avalanches and forces on a wall-like obstacle. Granul Matter 14:577–587. https://doi.org/10.1007/s10035-012-0358-8

Caccamo P, Faug T, Bellot H, Naaim-Bouvet F (2011) Experiments on a dry granular avalanche impacting an obstacle: dead zone, granular jump and induced forces. WIT Trans. Built Environ.

Calder E (2005) M.J. Branney and P. Kokelaar. Pyroclastic Density Currents and the Sedimentation of Ignimbrites. London (Geological Society). 2003. ISBN 1-86239-124-6, Price £65.00. Mineral Mag 69:220–221. https://doi.org/10.1180/s0026461x00024750

Calder ES, Cole PD, Dade WB, et al (1999) Mobility of pyroclastic flows and surges at the Soufriere Hills Volcano, Montserrat. Geophys Res Lett 26:537–540. https://doi.org/10.1029/1999gl900051

Charbonnier SJ, Germa A, Connor CB, et al (2013) Evaluation of the impact of the 2010 pyroclastic density currents at Merapi volcano from high-resolution satellite imagery, field investigations and numerical simulations. J Volcanol Geotherm Res 261:295–315. https://doi.org/10.1016/j.jvolgeores.2012.12.021

Charbonnier SJ, Gertisser R (2008) Field observations and surface characteristics of pristine block-and-ash flow deposits from the 2006 eruption of Merapi Volcano, Java, Indonesia. J Volcanol Geotherm Res 177:971–982. https://doi.org/10.1016/j.jvolgeores.2008.07.008

Charbonnier SJ, Thouret J-C, Gueugneau V, Constantinescu R (2020) New Insights Into the 2070calyrBP Pyroclastic Currents at El Misti Volcano (Peru) From Field Investigations, Satellite Imagery and Probabilistic Modeling. Front Earth Sci 8: 557788. https://doi.org/10.3389/feart.2020.557788

Charbonnier SJ, Gertisser R (2011) Deposit architecture and dynamics of the 2006 block-and-ash flows of Merapi Volcano, Java, Indonesia. Sedimentology 58:1573–1612. https://doi.org/10.1111/j.1365-3091.2011.01226.x

Chédeville C, Roche O (2015) Influence of slope angle on pore pressure generation and kinematics of pyroclastic flows: insights from laboratory experiments. Bull Volcanol 77:96. https://doi.org/10.1007/s00445-015-0981-4

Cole PD, Neri A, Baxter PJ (2015) Hazards from Pyroclastic Density Currents, Second Edi. Elsevier Inc.

Cui X, Gray JMNT, Jóhannesson T (2007) Deflecting dams and the formation of oblique shocks in snow avalanches at Flateyri, Iceland. J Geophys Res 112: F04012. https://doi.org/10.1029/2006jf000712

Doronzo DM, Valentine GA, Dellino P, de Tullio MD (2010) Numerical analysis of the effect of topography on deposition from dilute pyroclastic density currents. Earth Planet Sci Lett 300:164–173. https://doi.org/10.1016/j.epsl.2010.10.003

Druitt TH (1998) Pyroclastic density currents. Geol Soc London, Spec Publ 145:145–182. https://doi.org/10.1144/gsl.sp.1996.145.01.08

Druitt TH, Avard G, Bruni G, et al (2007) Gas retention in fine-grained pyroclastic flow materials at high temperatures. Bull Volcanol 69:881–901. https://doi.org/10.1007/s00445-007-0116-7

Druitt TH, Bruni G, Lettieri P, Yates JG (2004) The fluidization behaviour of ignimbrite at high temperature and with mechanical agitation. Geophys Res Lett 31: L02604. https://doi.org/10.1029/2003gl018593

Druitt TH, Calder ES, Cole PD, et al (2002) Small-volume, highly mobile pyroclastic flows formed by rapid sedimentation from pyroclastic surges at Soufrière Hills Volcano, Montserrat: an important volcanic hazard. Geol Soc London, Mem 21:263–279. https://doi.org/10.1144/gsl.mem.2002.021.01.12

Dufek J, Esposti Ongaro T, Roche O (2015) Pyroclastic Density Currents. Encycl. Volcanoes 617–629

Esposti Ongaro T, Cerminara M, Charbonnier SJ, et al (2020) A framework for validation and benchmarking of pyroclastic current models. Bull Volcanol 82:51. https://doi.org/10.1007/s00445-020-01388-2

Faug T, Caccamo P, Chanut B (2012) A scaling law for impact force of a granular avalanche flowing past a wall. Geophys Res Lett 39: L23401 . https://doi.org/10.1029/2012gl054112

Faug T (2021) Impact force of granular flows on walls normal to the bottom: Slow versus fast impact dynamics. Can Geotech J 58:114–124. https://doi.org/10.1139/cgj-2019-0399

Gertisser R, Cassidy NJ, Charbonnier SJ, et al (2011) Overbank block-and-ash flow deposits and the impact of valley-derived, unconfined flows on populated areas at Merapi volcano, Java, Indonesia. Nat Hazards 60:623–648. https://doi.org/10.1007/s11069-011-0044-x

Girolami L, Druitt TH, Roche O (2015) Towards a quantitative understanding of pyroclastic flows: Effects of expansion on the dynamics of laboratory fluidized granular flows. J Volcanol Geotherm Res 296:31–39. https://doi.org/10.1016/j.jvolgeores.2015.03.008

Gray JMNT, Cui X (2007) Weak, strong and detached oblique shocks in gravity-driven granular free-surface flows. J Fluid Mech 579:113–136. https://doi.org/10.1017/s0022112007004843

Gray JMNT, Tai Y-C, Noelle S (2003) Shock waves, dead zones and particle-free regions in rapid granular free-surface flows. J Fluid Mech 491:161–181. https://doi.org/10.1017/s0022112003005317

692 Gueugneau V, Kelfoun K, Roche O, Chupin L (2017) Effects of pore pressure in pyroclastic
693 flows: Numerical simulation and experimental validation. Geophys Res Lett 44:2194–2202.
694 https://doi.org/10.1002/2017GL072591

695 Gueugneau V, Charbonnier S, Esposti Ongaro T, et al (2021) Synthetic benchmarking of
696 concentrated pyroclastic current models. Bull Volcanol 83:75.
697 https://doi.org/10.1007/s00445-021-01491-y

698 Gueugneau V, Kelfoun K, Charbonnier S, et al (2020) Dynamics and Impacts of the May 8th,
699 1902 Pyroclastic Current at Mount Pelée (Martinique): New Insights From Numerical
700 Modeling. Front Earth Sci 8:279. https://doi.org/10.3389/feart.2020.00279

701 Gueugneau V, Kelfoun K, Druitt T (2019) Investigation of surge-derived pyroclastic flow
702 formation by numerical modelling of the 25 June 1997 dome collapse at Soufrière Hills
703 Volcano, Montserrat. Bull Volcanol 81:25. https://doi.org/10.1007/s00445-019-1284-y

704 Heyman J, Boltenhagen P, Delannay R, Valance A (2017) Experimental investigation of high
705 speed granular flows down inclines. EPJ Web Conf 140:3057.
706 https://doi.org/10.1051/epjconf/201714003057

707 Holyoake AJ, McElwaine JN (2012) High-speed granular chute flows. J Fluid Mech 710:35–71.
708 https://doi.org/10.1017/jfm.2012.331

709 Iverson RM, Vallance JW (2001) New views of granular mass flows. Geology 29:115.
710 https://doi.org/10.1130/0091-7613(2001)029<0115:nvogmf>2.0.co;2

711 Iverson RM, George DL, Logan M (2016) Debris flow runup on vertical barriers and adverse
712 slopes. J Geophys Res Earth Surf 121:2333–2357. https://doi.org/10.1002/2016JF003933

713 Jenkins S, Komorowski J-C, Baxter PJ, et al (2013) The Merapi 2010 eruption: An
714 interdisciplinary impact assessment methodology for studying pyroclastic density current
715 dynamics. J Volcanol Geotherm Res 261:316–329.
716 https://doi.org/10.1016/j.jvolgeores.2013.02.012

717 Jessop DE, Kelfoun K, Labazuy P, et al (2012) LiDAR derived morphology of the 1993 Lascar
718 pyroclastic flow deposits, and implication for flow dynamics and rheology. J Volcanol
719 Geotherm Res 245–246:81–97. https://doi.org/10.1016/j.jvolgeores.2012.06.030

720 Kelfoun K, Legros F, Gourgaud A (2000) A statistical study of trees damaged by the 22
721 November 1994 eruption of Merapi volcano (Java, Indonesia): relationships between ash-
722 cloud surges and block-and-ash flows. J Volcanol Geotherm Res 100:379–393.
723 https://doi.org/10.1016/s0377-0273(00)00147-5

724 Komorowski J-C, Jenkins S, Baxter PJ, et al (2013) Paroxysmal dome explosion during the
725 Merapi 2010 eruption: Processes and facies relationships of associated high-energy

pyroclastic density currents. J Volcanol Geotherm Res 261:260–294. https://doi.org/10.1016/j.jvolgeores.2013.01.007

Kubo Hutchison A, Dufek J (2021) Generation of Overspill Pyroclastic Density Currents in Sinuous Channels. J Geophys Res Solid Earth 126: e2021JB022442. https://doi.org/10.1029/2021jb022442

Lerner GA, Jenkins SF, Charbonnier SJ, et al (2022) The hazards of unconfined pyroclastic density currents: A new synthesis and classification according to their deposits, dynamics, and thermal and impact characteristics. J Volcanol Geotherm Res 421:107429. https://doi.org/10.1016/j.jvolgeores.2021.107429

Louge MY, Keast SC (2001) On dense granular flows down flat frictional inclines. Phys Fluids 13:1213–1233. https://doi.org/10.1063/1.1358870

Loughlin SC, Calder ES, Clarke A, et al (2002) Pyroclastic flows and surges generated by the 25 June 1997 dome collapse, Soufrière Hills Volcano, Montserrat. Geol Soc London, Mem 21:191–209. https://doi.org/10.1144/GSL.MEM.2002.021.01.09

Lube G, Cronin SJ, Thouret J-C, Surono (2011) Kinematic characteristics of pyroclastic density currents at Merapi and controls on their avulsion from natural and engineered channels. Geol Soc Am Bull 123:1127–1140. https://doi.org/10.1130/b30244.1

Lube G, ECP Breard, SJ Cronin, J Jones (2015) Synthesizing large-scale pyroclastic flows: Experimental design, scaling, and first results from PELE. J Geophys Res Solid Earth 120:1487–1502. doi:10.1002/2014JB011666.

Lube G, Breard ECP, Jones J, et al (2019) Generation of air lubrication within pyroclastic density currents. Nat Geosci 12:381–386. https://doi.org/10.1038/s41561-019-0338-2

Lube G, Breard ECP, Esposti-Ongaro T, et al (2020) Multiphase flow behaviour and hazard prediction of pyroclastic density currents. Nat Rev Earth Environ 1:348–365. https://doi.org/10.1038/s43017-020-0064-8

Lube G, Cronin SJ, Platz T, et al (2007) Flow and deposition of pyroclastic granular flows: A type example from the 1975 Ngauruhoe eruption, New Zealand. J Volcanol Geotherm Res 161:165–186. https://doi.org/10.1016/j.jvolgeores.2006.12.003

Mancarella D, Hungr O (2010) Analysis of run-up of granular avalanches against steep, adverse slopes and protective barriers. Can Geotech J 47:827–841. https://doi.org/10.1139/T09-143

Nairn IA, Self S (1978) Explosive eruptions and pyroclastic avalanches from Ngauruhoe in February 1975. J Volcanol Geotherm Res 3:39–60. https://doi.org/10.1016/0377-0273(78)90003-3

Nakada S, Fujii T (1993) Preliminary report on the activity at Unzen Volcano (Japan), November 1990-November 1991: Dacite lava domes and pyroclastic flows. J Volcanol Geotherm Res 54:319–333. https://doi.org/10.1016/0377-0273(93)90070-8

Ogburn SE, Calder ES, Cole PD, Stinton AJ (2014) Chapter 10 The effect of topography on ash-cloud surge generation and propagation. Geol Soc London, Mem 39:179–194. https://doi.org/10.1144/m39.10

Peruzzetto M, Mangeney A, Bouchut F, Grandjean G, Levy C, Thiery Y, Lucas A. (2021) Topography curvature effects in thin-layer models for gravity driven flows without bed erosion J Geophys Res Solid Earth 126:e2020JF005657. https://doi.org/10.1029/2020JF005657

Pollock NM, Brand BD, Rowley PJ, et al (2019) Inferring pyroclastic density current flow conditions using syn-depositional sedimentary structures. Bull Volcanol 81:46. https://doi.org/10.1007/s00445-019-1303-z

Pouliquen O (1999) On the shape of granular fronts down rough inclined planes. Phys Fluids 11:1956–1958. https://doi.org/10.1063/1.870057

Pudasaini SP, Hutter K, Hsiau S-S, et al (2007) Rapid flow of dry granular materials down inclined chutes impinging on rigid walls. Phys Fluids 19:53302. https://doi.org/10.1063/1.2726885

Roche O, Montserrat S, Niño Y, Tamburrino A (2010) Pore fluid pressure and internal kinematics of gravitational laboratory air-particle flows: Insights into the emplacement dynamics of pyroclastic flows. J Geophys Res 115: B09206. https://doi.org/10.1029/2009jb007133

Roche O, van den Wildenberg S, Valance A, et al (2021) Experimental assessment of the effective friction at the base of granular chute flows on a smooth incline. Phys Rev E 103: 042905. https://doi.org/10.1103/physreve.103.042905

Rowley PJ, Roche O, Druitt TH, Cas R (2014) Experimental study of dense pyroclastic density currents using sustained, gas-fluidized granular flows. Bull Volcanol 76:855. https://doi.org/10.1007/s00445-014-0855-1

Savage SB, Hutter K (1989) The motion of a finite mass of granular material down a rough incline. J Fluid Mech 199:177–215. https://doi.org/10.1017/s0022112089000340

Smith GM, Williams R, Rowley PJ, Parsons DR (2018) Investigation of variable aeration of monodisperse mixtures: implications for pyroclastic density currents. Bull Volcanol 80:67. https://doi.org/10.1007/s00445-018-1241-1

Smith G, Rowley P, Williams R, et al (2020) A bedform phase diagram for dense granular currents. Nat Commun 11:1–11. https://doi.org/10.1038/s41467-020-16657-z

794 Sparks RSJ (1978) Gas release rates from pyroclastic flows: a assessment of the role of
795 fluidisation in their emplacement. Bull Volcanol 41:1–9.
796 https://doi.org/10.1007/bf02597679

797 Sparks RSJ, Gardeweg MC, Calder ES, Matthews SJ (1997) Erosion by pyroclastic flows on
798 Lascar Volcano, Chile. Bull Volcanol 58:557–565. https://doi.org/10.1007/s004450050162

799 Sulpizio R, Castioni D, Rodriguez-Sedano LA, et al (2016) The influence of slope-angle ratio on
800 the dynamics of granular flows: insights from laboratory experiments. Bull Volcanol 78:77.
801 https://doi.org/10.1007/s00445-016-1069-5

802 Thielicke W, Sonntag R (2021) Particle Image Velocimetry for MATLAB: Accuracy and
803 enhanced algorithms in PIVlab. J Open Res Softw 9:12. https://doi.org/10.5334/jors.334

804 Tiberghien D, Laigle D, Naaim M, et al (2007) Experimental investigations of interaction
805 between mudflow and an obstacle. Int Conf Debris-Flow Hazards Mitig Mech Predict
806 Assessment, Proc 281–292

807 Valentine GA (1987) Stratified flow in pyroclastic surges. Bull Volcanol 49:616–630.
808 https://doi.org/10.1007/bf01079967

809 Valentine GA (2020) Initiation of dilute and concentrated pyroclastic currents from collapsing
810 mixtures and origin of their proximal deposits. Bull Volcanol 82:20.
811 https://doi.org/10.1007/s00445-020-1366-x

812 Wilson CJN (1980) The role of fluidization in the emplacement of pyroclastic claws: An
813 experimental approach. J Volcanol Geotherm Res 8:231–249. https://doi.org/10.1016/0377-
814 0273(80)90106-7

815 Wilson L, Head JW (1981) Morphology and rheology of pyroclastic flows and their deposits,
816 and guideline for future observations. U. S. Geol Surv Prof Pap 1250:513–524.
817 https://ci.nii.ac.jp/naid/10010385751/

818 Woods AW, Bursik MI, Kurbatov A V (1998) The interaction of ash flows with ridges. Bull
819 Volcanol 60:38–51. https://doi.org/10.1007/s004450050215

820 Yamamoto T, Takarada S, Suto S (1993) Pyroclastic flows from the 1991 eruption of Unzen
821 volcano, Japan. Bull Volcanol 55:166–175. https://doi.org/10.1007/bf00301514

822 Zanuttigh B, Lamberti A (2007) Instability and surge development in debris flows. Rev Geophys
823 45:RG3006. https://doi.org/10.1029/2005RG000175

824 Zhu C, Chen Z, Huang Y (2021) Coupled Moving Particle Simulation–Finite-Element Method
825 Analysis of Fluid–Structure Interaction in Geodisasters. Int J Geomech 21: 04021081.
826 https://doi.org/10.1061/(asce)gm.1943-5622.0002041

827 Zhu Y, Delannay R, Valance A (2020) High-speed confined granular flows down smooth
828 inclines: scaling and wall friction laws. Gran. Matt. 22:82. https://doi.org/10.1007/s10035-
829 020-01053-7

830

831

Fig1

a. channel bend
b. break in slope
c. obstacle in the valley
d. valley width constriction

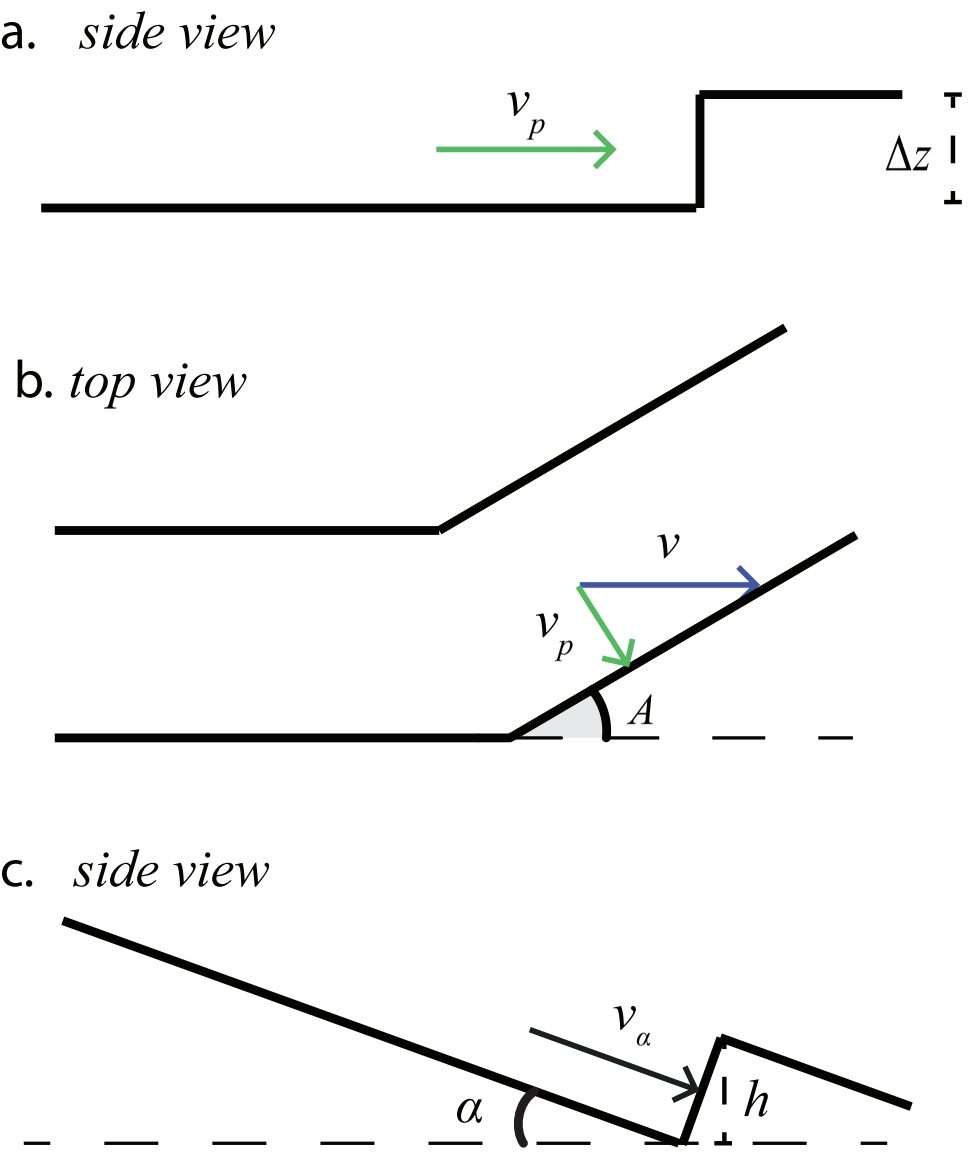
a. side view
v_p
Δz
b. top view
v
v_p
A
c. side view
v_α
α
h

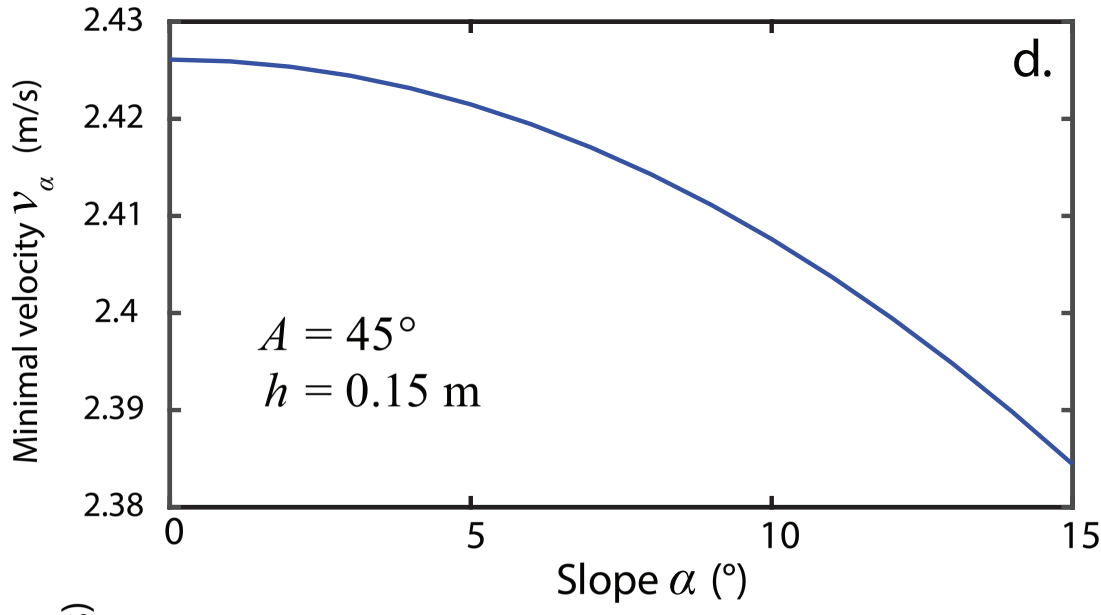
d.
Minimal velocity v_α (m/s)
2.43
2.42
2.41
2.4
2.39
2.38
$A = 45°$
$h = 0.15$ m
0
5
10
15
Slope α (°)

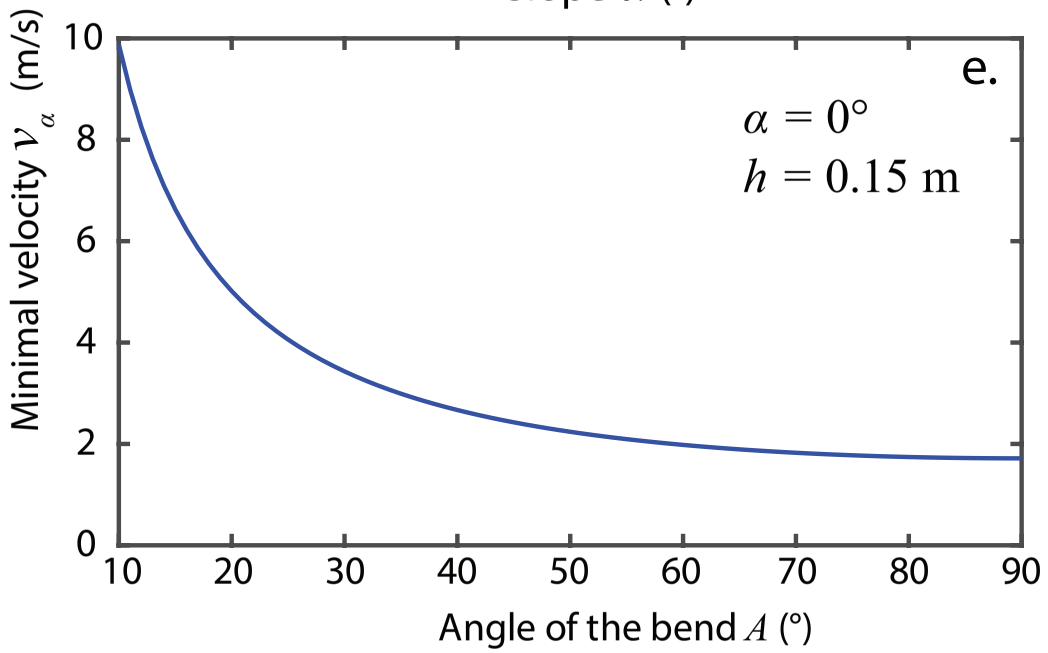
e.
Minimal velocity v_α (m/s)
10
8
6
4
2
0
$\alpha = 0°$
$h = 0.15$ m
10
20
30
40
50
60
70
80
90
Angle of the bend A (°)

a.


PYROCLAST

b.

c.

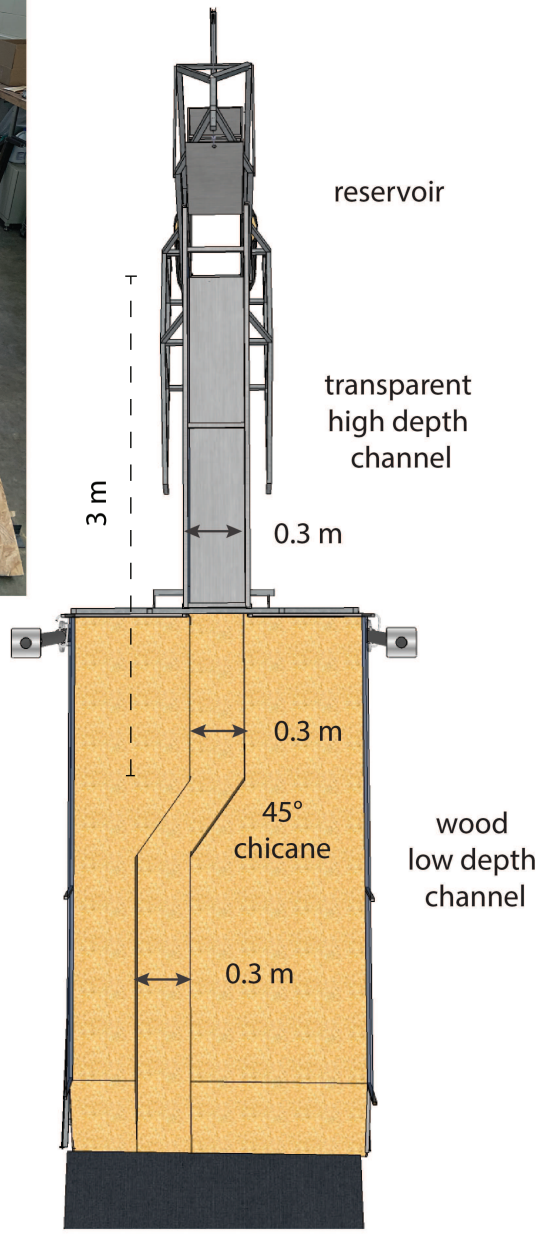
TOP
reservoir
transparent
high depth
channel
3 m
0.3 m
0.3 m
45°
chicane
wood
low depth
channel
0.3 m
Large banks to receive overbanking flow

d.

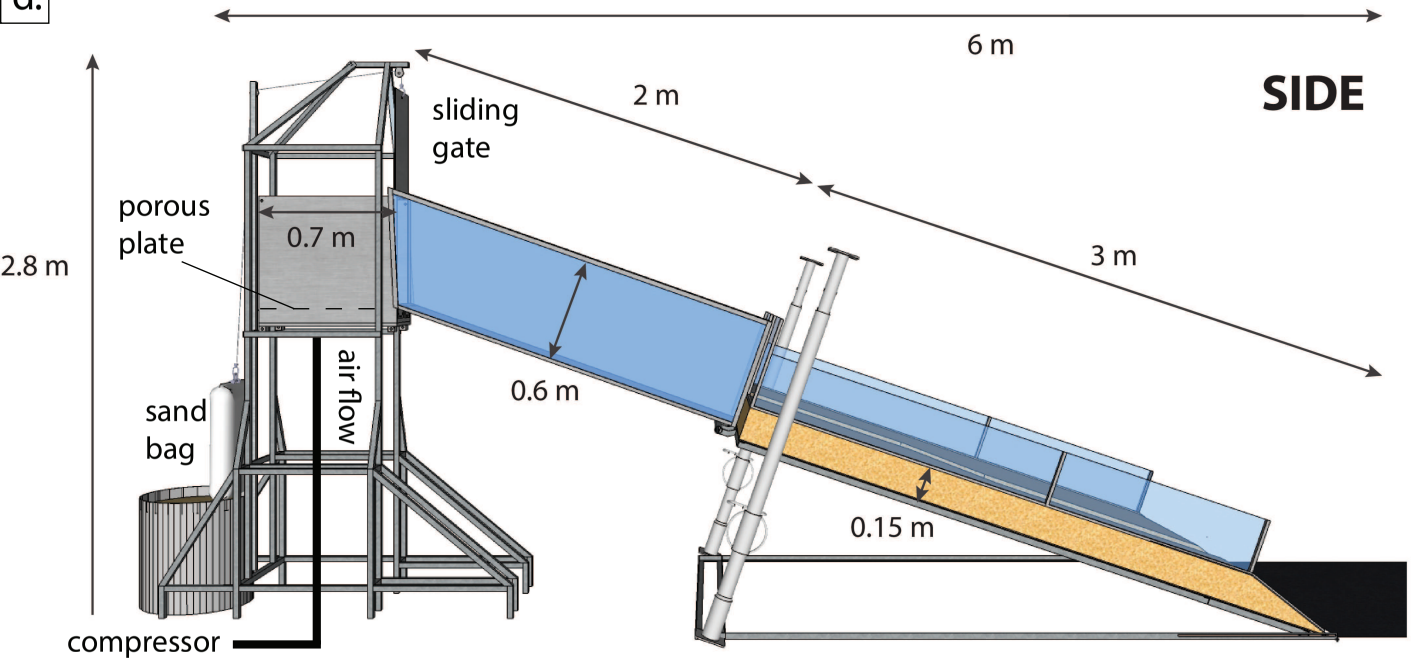
6 m
SIDE
2 m
sliding
gate
porous
plate
0.7 m
2.8 m
3 m
air flow
sand
bag
0.6 m
0.15 m
compressor

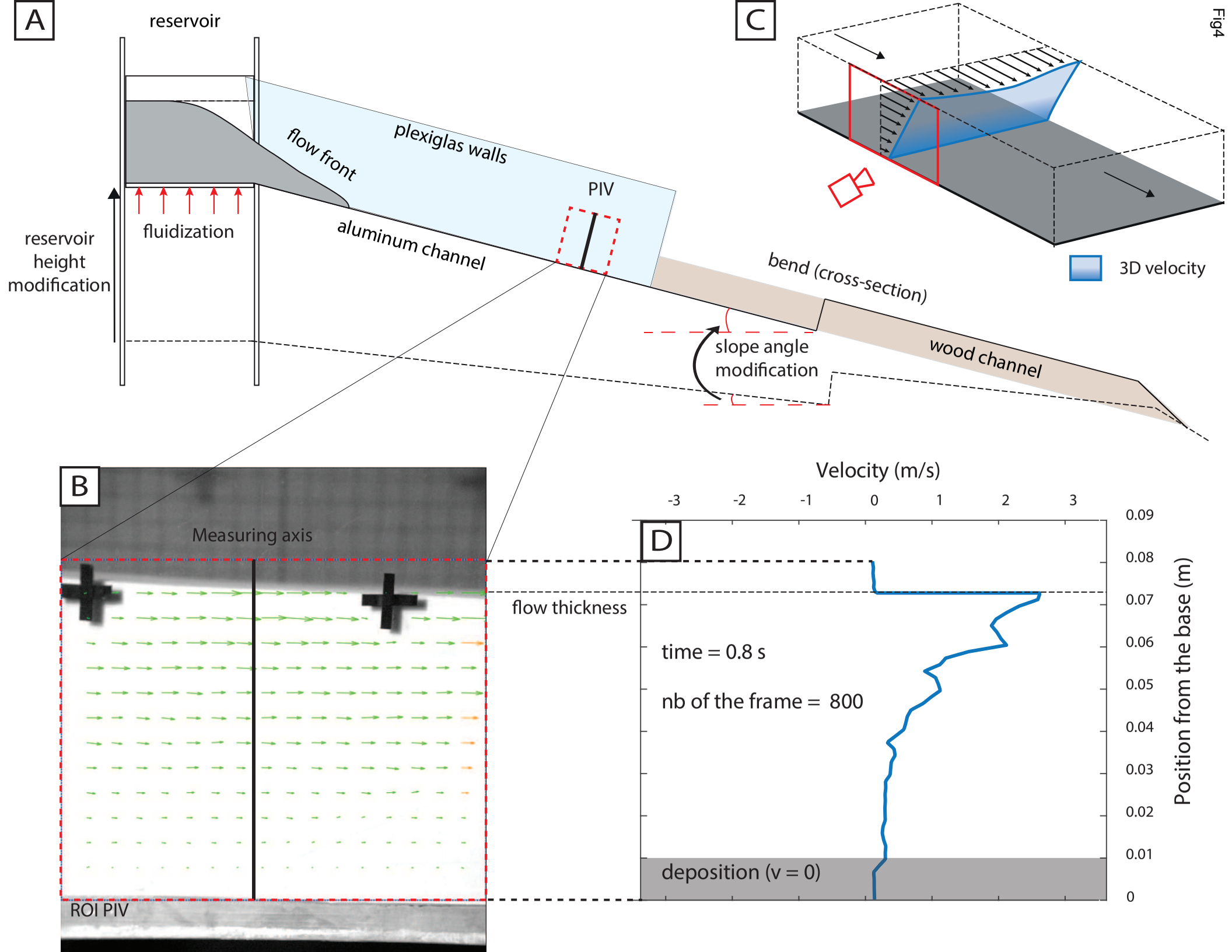
A
reservoir
flow front
plexiglas walls
PIV
fluidization
aluminum channel
reservoir
height
modification
bend (cross-section)
slope angle
modification
wood channel
C
3D velocity
Fig4
B
Measuring axis
flow thickness
ROI PIV
D
Velocity (m/s)
-3
-2
-1
0
1
2
3
time = 0.8 s
nb of the frame = 800
deposition (v = 0)
0.09
0.08
0.07
0.06
0.05
0.04
0.03
0.02
0.01
0
Position from the base (m)

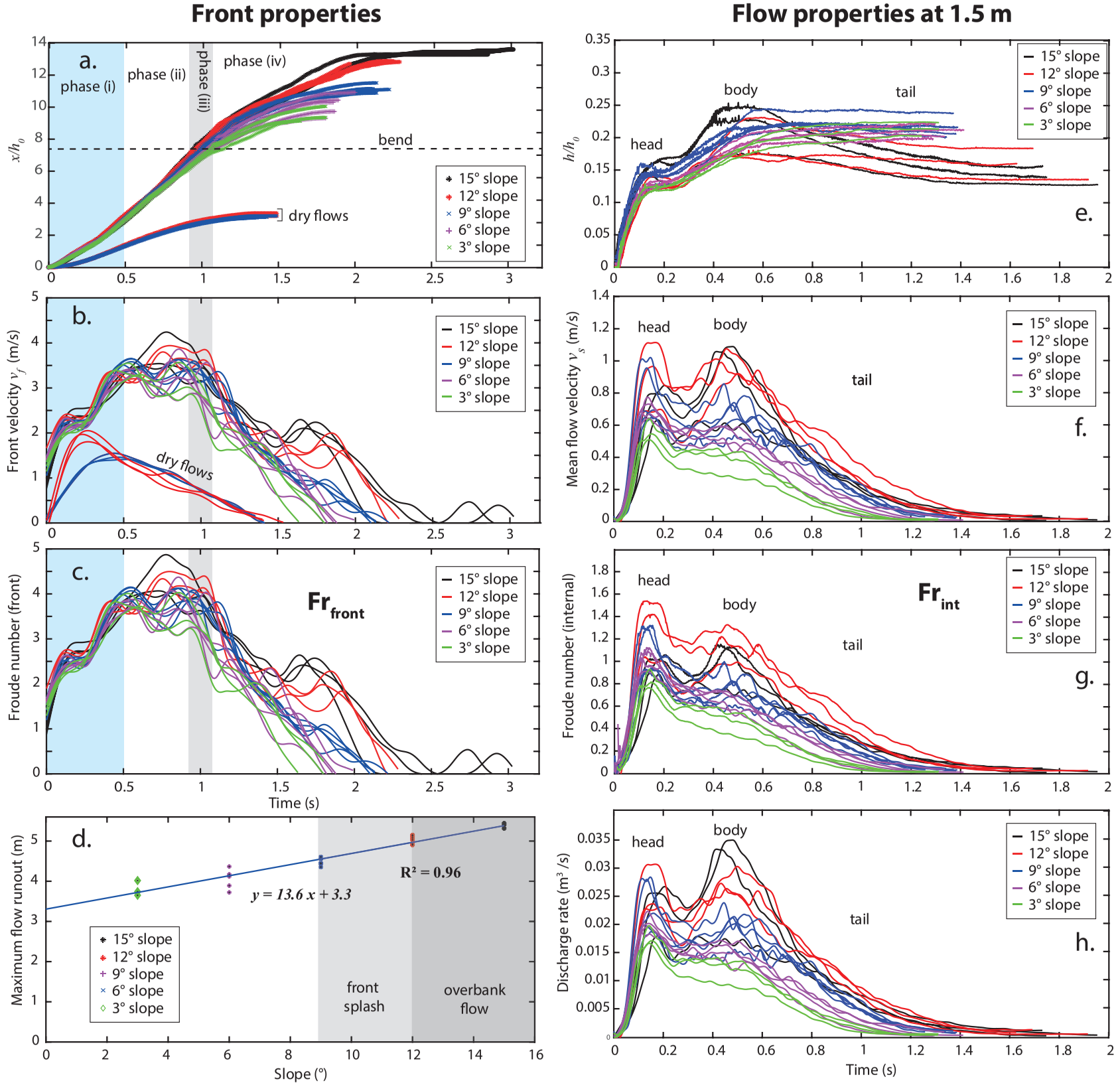
Front properties
Flow properties at 1.5 m
a.
phase (i)
phase (ii)
phase (iii)
phase (iv)
bend
dry flows
x/h0
15° slope
12° slope
9° slope
6° slope
3° slope
b.
Front velocity vf (m/s)
dry flows
c.
Froude number (front)
Frfront
Time (s)
d.
Maximum flow runout (m)
R² = 0.96
y = 13.6 x + 3.3
front splash
overbank flow
Slope (°)
e.
h/h0
head
body
tail
f.
Mean flow velocity vs (m/s)
g.
Froude number (internal)
Frint
h.
Discharge rate (m³/s)
Time (s)

Fig5

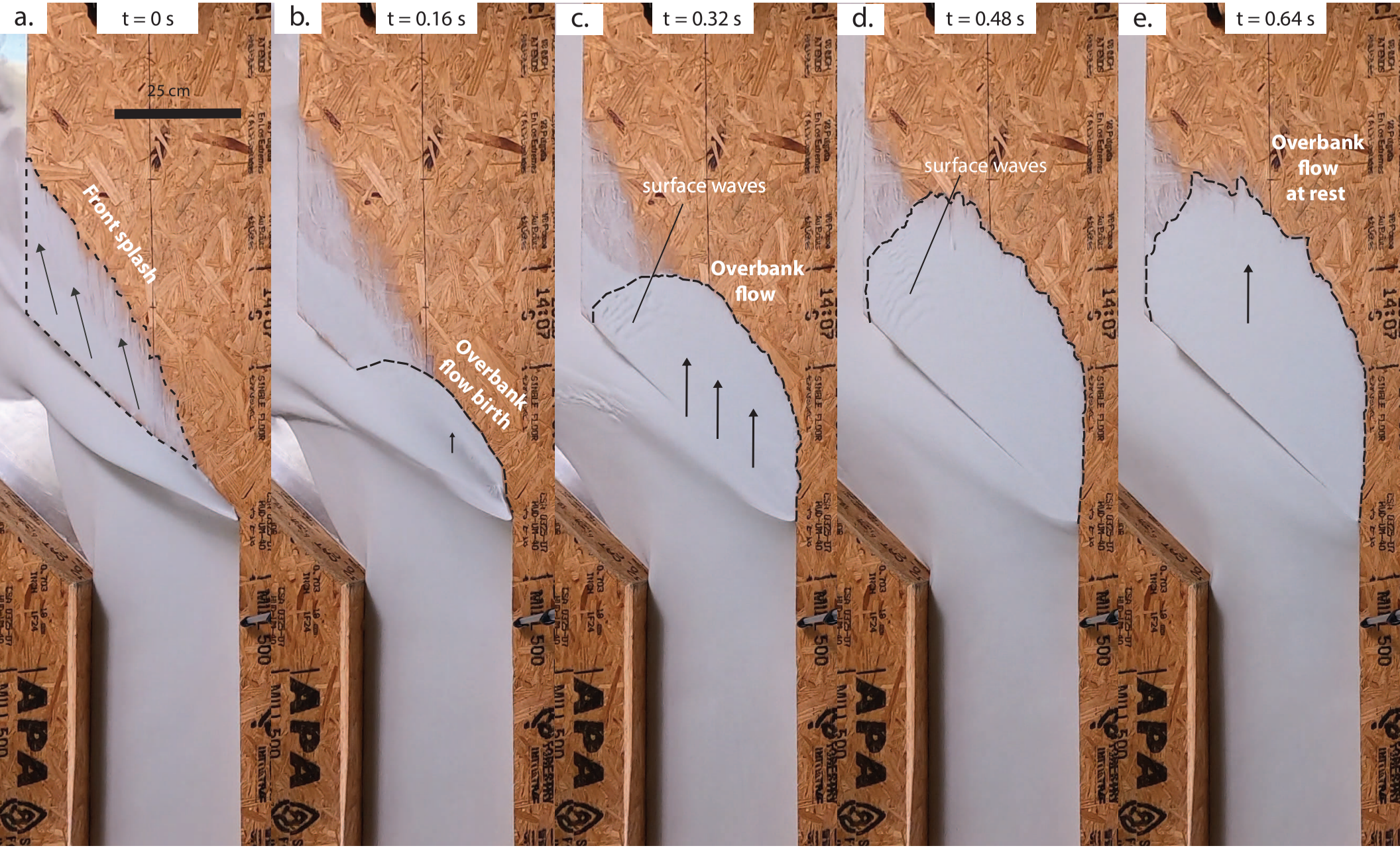
a.
t = 0 s
25 cm
Front splash
b.
t = 0.16 s
Overbank flow birth
c.
t = 0.32 s
surface waves
Overbank flow
d.
t = 0.48 s
surface waves
e.
t = 0.64 s
Overbank flow at rest

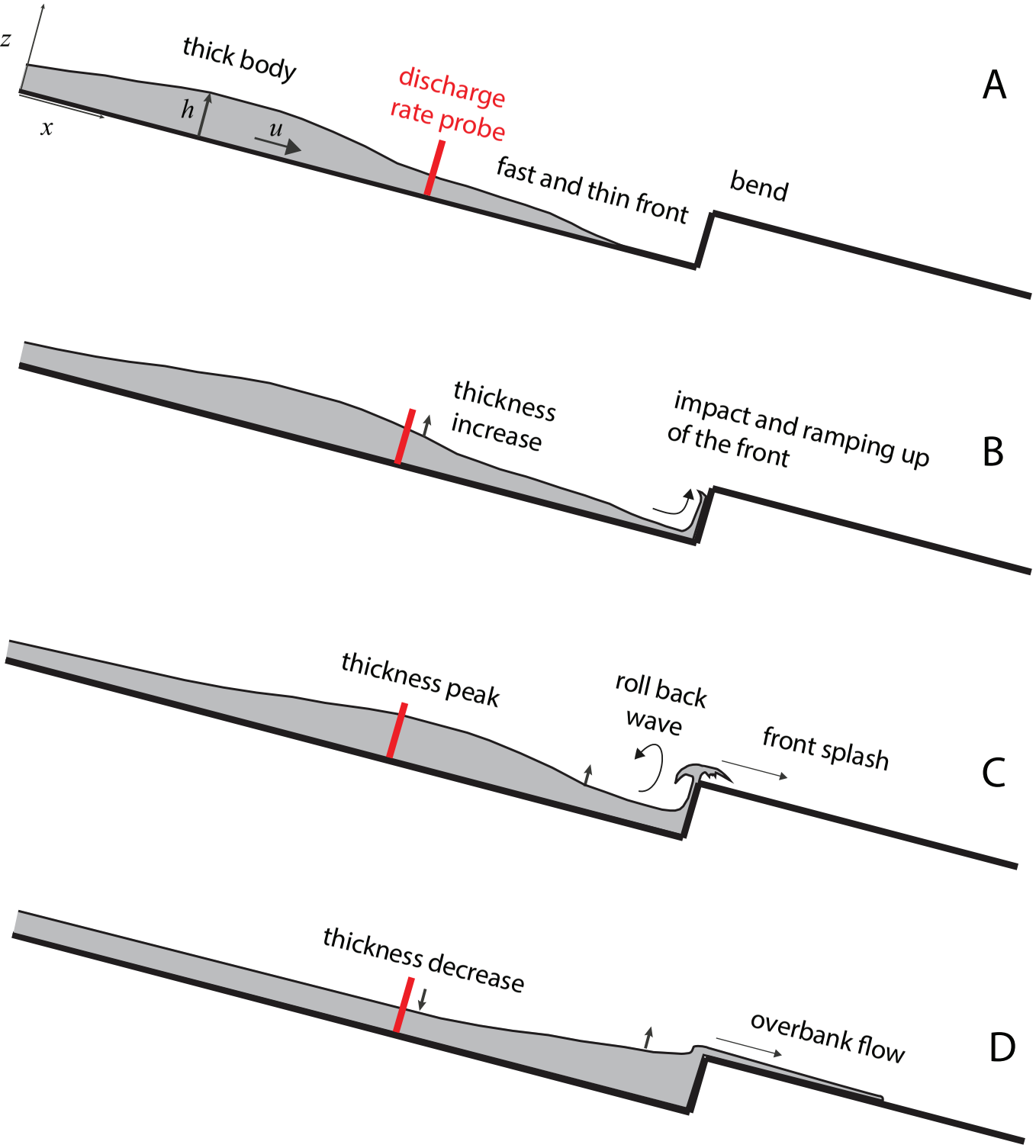
z
x
h
u
thick body
discharge
rate probe
fast and thin front
bend
A
thickness
increase
impact and ramping up
of the front
B
thickness peak
roll back
wave
front splash
C
thickness decrease
overbank flow
D

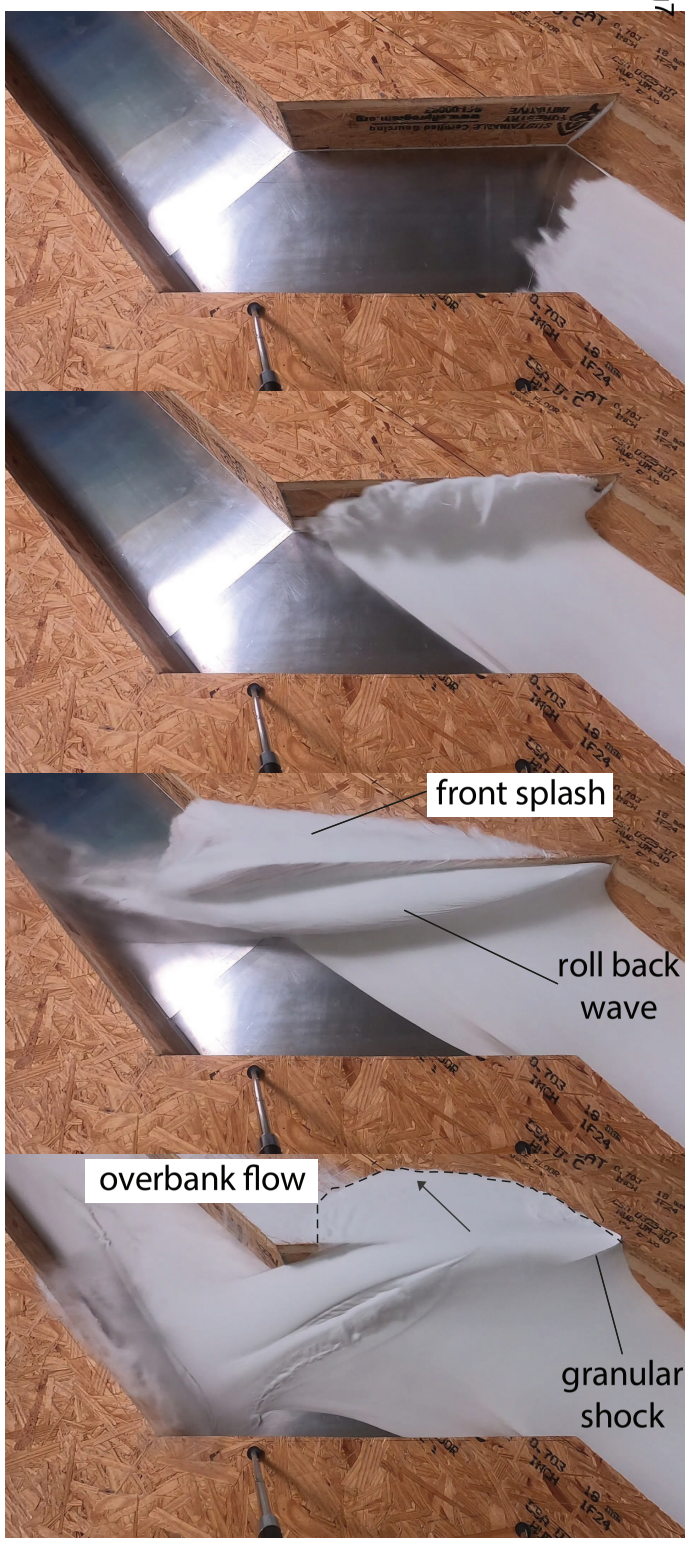
front splash
roll back
wave
overbank flow
granular
shock

Fig7

Fig8

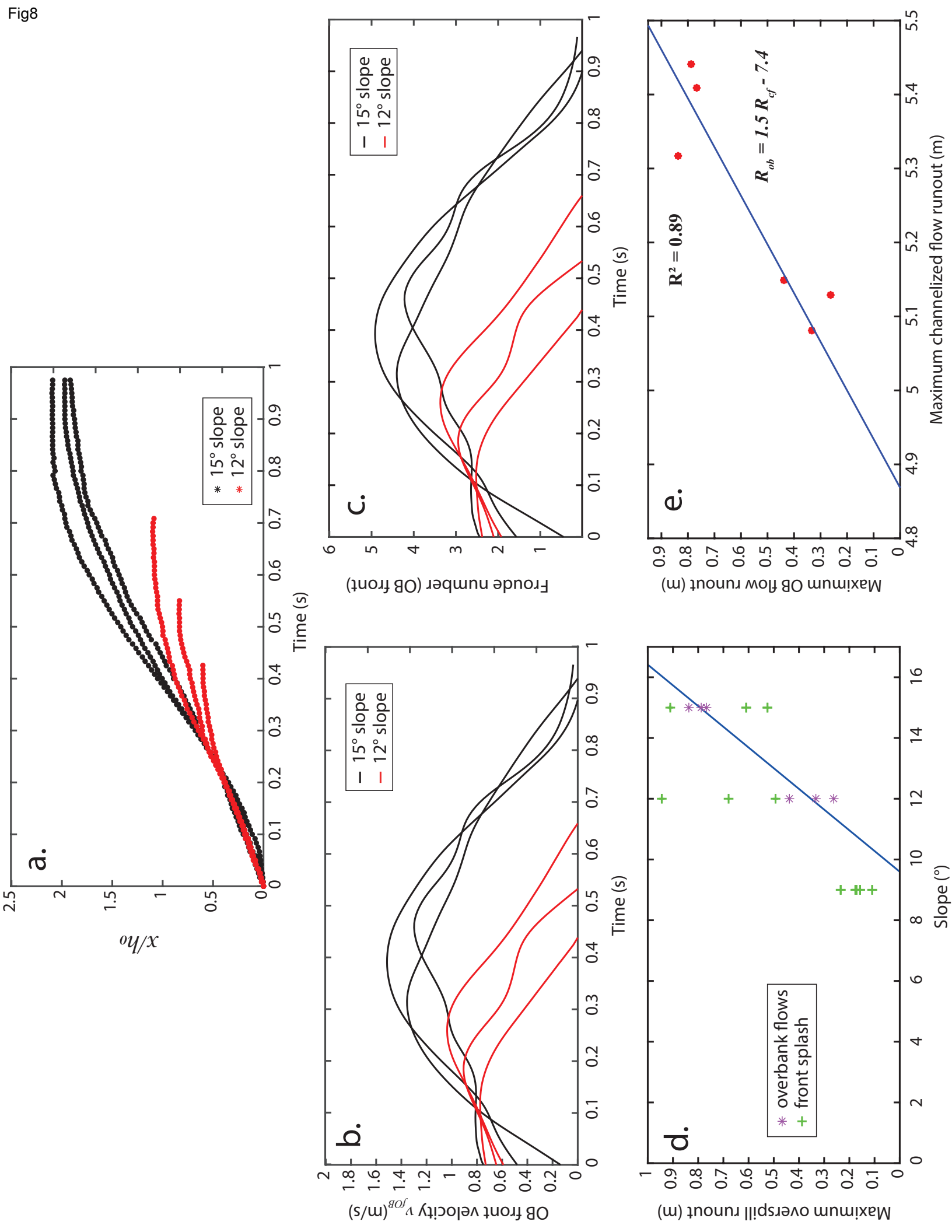
a.
15° slope
12° slope
x/h_o
b.
OB front velocity v_{fOB} (m/s)
Time (s)
c.
Froude number (OB front)
d.
Maximum overspill runout (m)
overbank flows
front splash
Slope (°)
e.
Maximum OB flow runout (m)
$R^2 = 0.89$
$R_{ob} = 1.5\,R_{cf} - 7.4$
Maximum channelized flow runout (m)

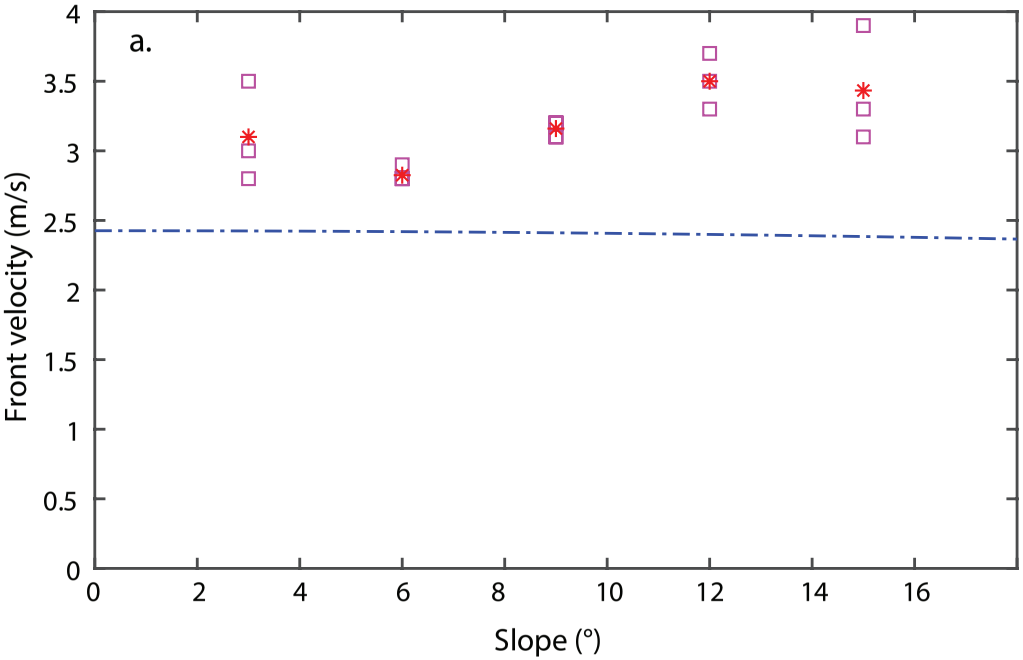
a.
Front velocity (m/s)
Slope (°)
0
0.5
1
1.5
2
2.5
3
3.5
4
0
2
4
6
8
10
12
14
16

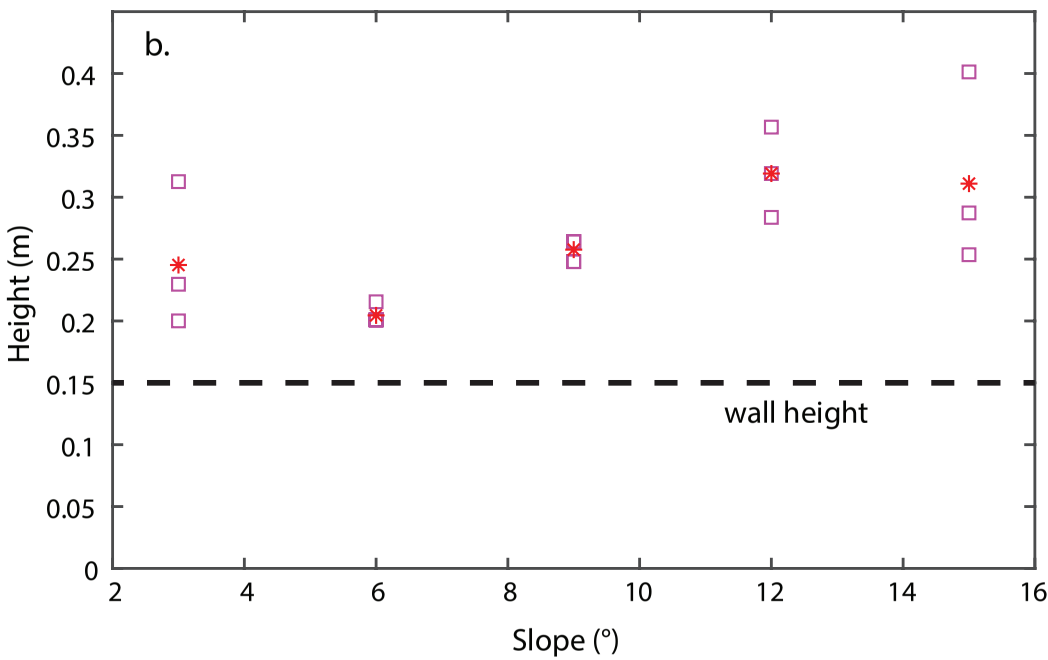
b.
Height (m)
Slope (°)
wall height
0
0.05
0.1
0.15
0.2
0.25
0.3
0.35
0.4
2
4
6
8
10
12
14
16

Table 1

Eruption	Topographic feature type	Distance of source to obstacle (km)	Flow runout distance (km)	Height/ Width obstacle	Ratio of distance of obstacle to flow runout	H/L flow	References
Colima 2015	Bend	3.5	10.4	0.33	0.33	0.28	Macorps et al. (2018)
SHV 1997	Bend	1.8	5.3	0.33	0.34	0.14	Loughlins et al. (2002); Ogburn et al. (2014)
Unzen 1991	Bend	1.6	7.2	0.22	0.22	0.31	Yamamoto et al. (1993); Fujii and Nakada (1999)
Merapi 1994	Break in slope	1.8	6.5	0.15	0.28	0.29	Bourdier and Abdurachman (2001); Kelfoun et al. (2000)
Merapi 2006	Obstacle + Constriction	4.5	7	0.39	0.64	0.28	Charbonnier and Gertisser (2008, 2011) ; Lube et al. (2011)
Merapi 2010	Bend + Constriction	1.8	16.2	0.15	0.11	0.16	Komorowski et al. (2013) ; Jenkins et al. (2013) ; Gertisser (2012)
Fuego 2018	Bend	7.8	11.4	0.29	0.68	0.26	Albino et al. (2020)
Ngauruhoe 1975	Break in slope	1.2	2.24	0.14	0.53	0.45	Nairn et Self (1978) ; Lube et al. (2007)
Lascar 1993	Constriction	1	6	0.16	0.17	0.29	Sparks et al. (1997) Jessop et al. (2012)
PyroCLAST	Bend	3 m	3.3-5.4 m	0.46	0.56-0.91	0.05-0.26	This study

Table 2

Dimensionless numbers	CPCs	PyroCLAST
Mass Number $Ma = \varepsilon_s \rho_s / (\varepsilon_f \rho_f)$	$10^2 – 10^3$	10^3
Froude number $Fr = v_f / (gh)^{1/2}$	1.6 – 3	2.3 – 3.4
Bagnold number $Ba = \varepsilon_s \rho_s v_f d^2 / (\varepsilon_f \mu)$	$10^1 – 10^2$	10^2
Darcy number $Da = \mu / (\varepsilon_s \rho_s \gamma k)$	$10^1 – 10^4$	$10^1 – 10^2$
Fluidization number $Fl = k\varepsilon_s(\rho_s - \rho_f)(g/L)^{1/2} / (\mu \varepsilon_f)$	$10^{-7} – 10^{-3}$	10^{-3}
Pore pressure number $Pr = (g/L)^{1/2} / (h^2 D)$	$10^{-4} – 10^1$	10^1
Inertial number $I = \gamma d / \sqrt{P/\rho_s}$	$10^{-5} – 10^{-4}$	10^{-3}

ε_f	Gas volume fraction
ε_s	Solid volume fraction
ρ_s	Density of the solid fraction (kg m^{-3})
ρ_f	Density of the fluid (kg m^{-3})
v_f	Flow front velocity (m s^{-1})
γ	Mean shear rate (s^{-1})
μ	Fluid dynamic viscosity (Pa s^{-1})
k	Permeability (m^2)
g	Gravity (m s^{-2})
L	Characteristic length (m)
D	Hydraulic diffusion coefficient (m^2 s^{-1})
h	Characteristic flow thickness (m)
α	Slope angle (degree)
d	Particle mean diameter (d_{43})
P	Normal stress